# BCAL Facts
# What we know and how we know

B. Leverington, G. Lolos, Z. Papandreou[1] and A. Semenov
University of Regina

S. Katsaganis and C. Kourkoumeli
University of Athens

A. Dzierba[1]
Indiana University

D. Lawrence
Jefferson Lab

*July 24, 2007*

## Abstract

This note summarizes what we know about the BCAL calorimeter and how we know it, based on analysis of data from beam tests in TRIUMF and JLab and cosmic rays and Monte Carlo simulations. The work related to this document is ongoing and it is expected that it will be finalized by the end of 2007.

[1]Corresponding authors: A. Dzierba and Z. Papandreou

# Overview

This note summarizes what we know about the BCAL calorimeter and how we know it, based on analysis of data from beam tests in TRIUMF and JLab and cosmic rays and Monte Carlo simulations. More information is available in the published literature and GlueX documents available on the GlueX portal. The GlueX barrel calorimeter (BCAL) is based on the design of the Pb/Sci electromagnetic calorimeter for the KLOE experiment [1, 2, 3, 4, 5, 6, 7, 8].

## The Mission of BCAL

Figure 1 shows a schematic of the proposed barrel calorimeter to be used inside the GlueX detector superconducting solenoid that produces a field of 2 T. The BCAL detector is essential for achieving the hermeticity and resolution required of the GlueX detector to carry out amplitude analyses of a large variety of exclusive reactions. The decay products of mesons produced in these reactions, including charged particles and photons, must be detected and measured with excellent acceptance and resolution. The task of BCAL is to measure the positions and energies of photons emitted from interactions in the GlueX target from 10° to 117° with respect to the beam direction. The photon position resolution of BCAL is determined by the resolution in the difference of arrival time between the two ends of the module. The timing information from BCAL will also be used to determine the time-of-flight information for charged particles entering BCAL after passing through layers of straw drift tubes (central drift chamber) surrounding the target.

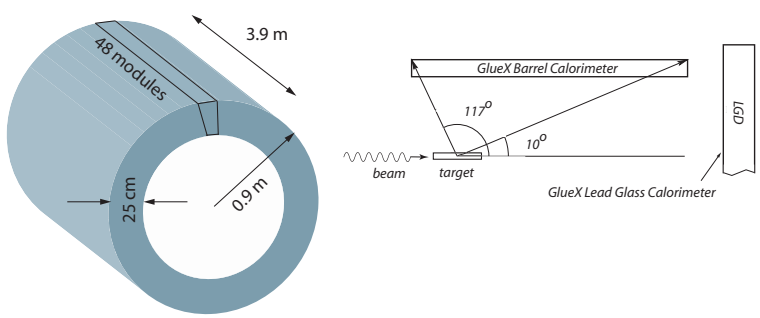


Figure 1: Schematic of the GlueX Barrel Calorimeter (BCAL) and its placement in the GlueX detector (not to scale).

BCAL will be 3.9 m long, with an outer radius of 0.9 m and an inner radius of 0.65 m. It will consist of 48 modules, each with a trapezoidal cross section. The modules will be constructed using scintillating fibers (SciFi) embedded in a lead (Pb) matrix. Such Pb/SciFi techniques have been employed in the construction of cylindrical electromagnetic calorimeters in the JetSet experiment at CERN and more recently in the KLOE experiment. Indeed the BCAL design draws heavily on the KLOE experience [3, 4] – the KLOE detector has 24 modules that are 4.3 m long and 23 cm thick, operating in a field of 0.6 T. The design of the BCAL is very similar to the KLOE electromagnetic calorimeter which had a reported energy resolution of $5.4\%/\sqrt{E(GeV)}$ plus a negligible constant term and a timing resolution of 54 ps$/\sqrt{E(GeV)}\oplus$140 ps [3, 4]. GlueX expects similar resolutions for the BCAL.

Compared to the KLOE experiment, the photon trajectories in GlueX present more of a challenge for energy and spatial measurements. The KLOE calorimeter subtends polar angles between 49° and 131°, a region that has an approximately uniform population of photons. Measured with respect to the normal to calorimeter modules, the angular range is between 0° and 41°. In contrast, the photons to be detected by BCAL (see Figure 1) have angles of incidence, measured with respect to the normal, from 0° to 170° with a much larger population near the larger angles – these photons coming from the decays of mesons that are preferentially produced in the forward direction. The energy and position measurement of photons at large angles of incidence were a primary goal of the BCAL beam tests carried out in Hall-B in September 2006.

## BCAL Prototype Module

Several prototype modules of the BCAL have been constructed. The first full-size module (Module 1), consists of alternating layers of thin (0.5 mm) lead sheets and 1-mm-diameter, dual-clad, scintillating fibers (SciFi) from Pol.Hi.Tech. with peak emission wavelength of 420 nm. The lead sheets are plastically deformed after passing through a specially-designed swaging machine. The fibers are glued manually in the resulting grooves with an optical epoxy. The resulting matrix has a design fiber pitch of 1.35 mm in the horizontal direction and 1.18 mm in the vertical. The dimensions of Module 1 are: $13 \times 23 \times 400$ cm$^3$ (width x thickness x length). The thickness of the module in radiation lengths is 15.5. The sampling frequency derived from its ∼220 layers of SciFi. The properties and features of the BCAL are summarized in Table 1.

The Pb:SciFI:Glue ratios for the module are 37:49:14 leading to a radiation length of 1.45 cm. Details leading to the radiation length estimates are given in [11]. For more details, the reader is directed to references [11, 12, 13, 14].

## BCAL Beam Test with Charged Particles at TRIUMF

A beam test was performed using Module 1 at TRIUMF's M11 area in June 2005, together with prototypes of the Time of Flight modules in collaboration with Indiana University. The goal of the beam test was to study the behavior of BCAL and make a first evaluation of several of its characteristics, such as the time and energy resolution, effective speed of light and light attenuation.

The module was placed with its long side perpendicular to the beam and its 23 cm side along the beam direction. Two beam momenta were used - 120 MeV/c at 18 Hz and 250 MeV/c at 22 Hz, with positrons, positive muons and positive pions present in the beam. A z-position scan was carried out with the beam always perpendicular to the long side of the module.

The incoming beam first goes through a smal, thin scintillator counter (called 'shortie') with 1 cm thickness, which is the starting point for counting time for all systems. Then the particles go through a $1 \times 1 \times 1$ cm$^3$ scintillator piece (called 'cubie'), which together with the shortie is used as a trigger. Next come the two scintillator bars of the Time of Flight with 1 cm thickness, with their long sides parallel to the Module-1 long side. Lastly, the beam struck was Module-1.

| **Property** | **Symbol** | **Value** |
|---|---|---|
| Module Length | $L$ | 390 cm |
| Module Inner Cord | $c_i$ | 8.51 cm |
| Module Outer Cord | $c_o$ | 11.77 cm |
| Module Thickness | $d$ | 22.5 cm |
| Module Azimuthal Bite | $\Delta\phi$ | $7.5^o$ |
| Radial Fiber Pitch | $p_r$ | 1.18 mm |
| Azimuthal Fiber Pitch | $p_\phi$ | 1.35 mm |
| Volume Ratios | Pb:SciFi:Glue | 37:49:14 |
| Effective Mass Number | $A_{eff}$ | 179.9 |
| Effective Atomic Number | $Z_{eff}$ | 71.4 |
| Effective Density | $\rho_{eff}$ | 4.88 g/cm$^3$ |
| Effective Speed of Light | $v_{eff}$ | ~16 cm/ns |
| Critical Energy | $E_c$ | 11.02 MeV [9], 8.36 MeV [10] |
| Radiation Length | $X_0$ | 7.06 g/cm$^2$ or 1.45 cm |
| No of Radiation Lengths | n$X_0$ | $15.5X_0$ (total thickness) |
| Max Shower | $t_{max}$ | $5.0X_0$ [9], $5.3X_0$ [10] (at 1 GeV) |
| 95% Shower | $t_{95\%}$ | $20.3X_0$ [9], $20.6X_0$ [10] (at 1 GeV) |
| Molière Radius | $R_M$ | 17.7 g/cm$^2$ or 3.63 cm [10] |
| Energy Resolution | $\frac{\sigma_E}{E}$ | $5\%/\sqrt{E} \oplus 1\%$ |
| Timing Resolution | $\sigma_t$ | 60 ps$/\sqrt{E} \oplus$ 150 ps |
| Position Resolution | $\sigma_{pos}$ | 5 mm$/\sqrt{E}$ (weighted) |
| Azimuthal Resolution | $\sigma_\phi$ | $\sim$ 8.5 mrad |
| Polar Resolution | $\sigma_\theta$ | $\sim$ 20 mrad (at $\theta = 45^o$) |

Table 1: List of the BCAL's properties and features.

Module-1 had four PMT units attached - two on each side, and the two upstream the beam will be further called Front (Left or Right), and the two downstream will be further called Back (Left or Right). The light guides covered an area of $10 \times 10$ cm$^2$, from 1.5 cm to 11.5 cm along the 13 cm side (Fig. 2). The light guides of the Front PMTs cover the first ten centimeters of depth from the face on which the beam is insident, and the light guides of the Back PMTs cover the next ten centimeters (the last three centimeters were not covered, but Monte Carlo simulations show that no more than 1% of the energy is deposited there for the particle energies used during the TRIUMF test).

The data analysis procedure for positrons for the two measured energies and muons for 120 MeV/c, and the raw results from each channel and for combination of channels (e.g. the Mean Timer) are presented in this section. Pions were not analyzed for either energy, because of the small fraction in the 120 MeV/c sample and the impossibility to spearate them from muons in the 250 MeV/c sample. For the latter reason muons in the 250 MeV/c sample were also not analyzed.

Data were taken with positrons, muons, and pions present in the beam, and a clear separation of the peaks of the three types of particles could be seen in the TOF data (Fig.3) in the 120 MeV/c samples. One of the goals of the analysis was to separate the types of particles. There was no clear separation of muons from pions in the 250 MeV/c runs. At each z-position of the BCAL several

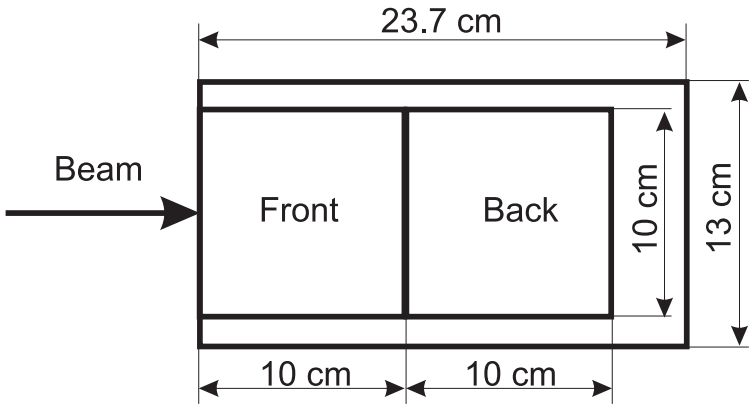


Figure 2: Attachment of the light guides on one side of the module during the TRIUMF 2005 tests.

runs of 15000 triggered events were taken, and the positions of the BCAL were changed by sliding it in steps of 10 or 20 cm along its 4-m length. Points from the center of the module (z=200 cm) up to 20 cm from the Left edge (z=20 cm) were recorded.

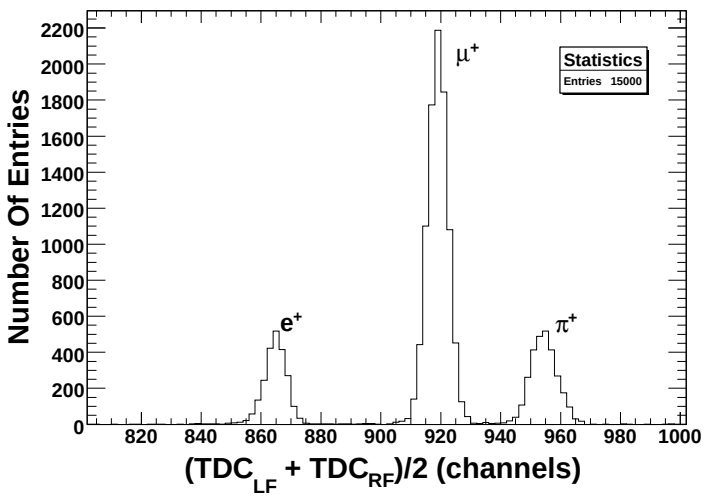


Figure 3: Particle separation at 120 MeV/c from TOF at TRIUMF.

The pedestals of each ADC were fitted with a Gaussian for each run and the channel number of the peak was subtracted from the ADC channel for each event. Next, walk corrections were applied to the TDCs, on a run-by-run basis, using the following formula:

$$t_{corr} = t_{meas} - \frac{w}{\sqrt{ADC}} \tag{1}$$

Here the weight $w$ is a coefficient determined by fitting the two dimensional plot of the TDC versus ADC signals, with the high-amplitude events, for which no walk correction was need, taken as the reference point.

For each run both TDC and ADC values were subjected to upper and lower limit cuts, in order to eliminate very few events with very untypical values, which could deteriotate the distributions

(long-range tails). Many combinations of cuts were tried in order to make sure that the final results do not vary more than 1-2% when varying the cuts. After the walk correction is done, the TDC data for each run was fitted with a Gaussian. Likewise, the ADC data for each channel were fitted with a Gaussian for the 120 MeV/c positrons and for the front ADCs of the 250 MeV/c positrons, while a Moyal fit was used for the 120 MeV muons and the back ADCs of the 250 MeV/c positrons.

As a next step in the analysis four more quantities were formed and analyzed - the Mean Timer (MT) of the TDC signals, the Geometric Mean (GM) of the ADC signals (these latter two are done on an event by event basis), the Time Difference (TD) of the TDC signals, and the Ratio (R) of the ADC signals (these two are done by using the averages over all events in a run). Their definitions, for each of the Front and Back sides separately, are the following:

$$MT(event) = TDC_{left}(event) + TDC_{right}(event)$$

$$GM(event) = \sqrt{ADC_{left}(event) * ADC_{right}(event)}$$

$$TD = TDC_{left}(mean) - TDC_{right}(mean)$$

$$R = \frac{ADC_{left}(mean)}{ADC_{right}(mean)}$$

MT provides a data quality check as it is approximately constant and related to the length of the module. TD provides information on the hit location of the incident particle. R results in the removal of geometrical factors of the collected scintillation light. Finally, GM is related to the energy deposited in the module and is independent of the z-position of the beam, thus effectively removing attenuation effects.

The GEANT Monte Carlo simulations were performed with the exact geometry of the beam test. Cutoff energies of 10 keV were used for both photons and electrons/positrons. Positrons and muons with five different momenta were simulated: 120 MeV/c, 250 MeV/c, 500 MeV/c, 1 GeV/c, and 2 GeV/c. In one set of runs the incident particles were started at the face of Module-1, not going through the scintillators of the Time of Flight setup, in order to investigate the influence of the spread of the hit position due to multiple scattering in these scintillators. The final goal for this chapter is to extract the best possible estimates of the time and energy resolution of Module-1.

The sampling fraction fluctuations are the dominant factor for the energy resolution of all sampling calorimeters. As a first Monte Carlo check the sampling fraction was calculated for all simulated energies. The results for positrons and muons, with and without the TOF, are presented in Table 2.

The sampling fraction for positrons w/o TOF is stable with values in the range 12.1-12.3% for all energies and corresponds well to previous Monte Carlo simulations [15]. The values are very slightly higher than the 11.9% reported by KLOE. The width of these distributions decreases with the insident energy, so the sampling fraction is more and more stable from event to event, which is of course exactly as expected. For the experimental results this means that we expect the larger variations in the sampling fraction for 120 MeV/c and to a lesser extent for 250 MeV/c to affect the energy resolution, since the sampling fraction is the major factor for it. The sampling fraction and width for positrons with the TOF increase slightly only for 120 MeV/c and 250 MeV/c. The sampling fractions for muons without and with the TOF units are higher than those of positrons and close to those reported by KLOE.

Table 2: Sampling fraction (SF) in Module-1 for positrons and muons from Monte Carlo with and without the TOF units.

| Momentum | Positrons w/o TOF | | Positrons w TOF | | Muons w/o TOF | | Muons w TOF | |
|---|---|---|---|---|---|---|---|---|
| (MeV/c) | SF (%) | $\sigma$ (%) | SF (%) | $\sigma$ (%) | SF (%) | $\sigma$ (%) | SF (%) | $\sigma$ (%) |
| 120 | 12.1 | 1.6 | 12.3 | 1.8 | 15.5 | 2.4 | 15.4 | 3.0 |
| 250 | 12.1 | 1.1 | 12.3 | 1.3 | 16.3 | 1.5 | 16.3 | 1.5 |
| 500 | 12.2 | 0.9 | 12.3 | 0.9 | 16.3 | 1.5 | 15.9 | 1.5 |
| 1000 | 12.3 | 0.7 | 12.3 | 0.7 | 14.8 | 2.2 | 15.0 | 2.1 |
| 2000 | 12.3 | 0.5 | 12.4 | 0.5 | 14.1 | 2.2 | 14.7 | 2.5 |

The behavior of the sampling fraction for muons with energy (first increasing and then decreasing again) can be explained in the following way. Muons at 120 MeV/c are close to mips (for which 16-17% sampling fraction is expected), but they decay and after that the energy deposited in the fibers will be less, as a usual positron initiated shower will be produced. Muons at 250 MeV/c and 500 MeV/c are still close to mips (most of the 250 MeV/c muons still decay in Module-1, but much later), so for them the sampling fraction is higher and within the expected range for mips. Muons in the GeV range no longer behave liks mips and respectively the sampling fraction decreases, but is still higher than the positron samples. The consistency of the sampling fraction Monte Carlo simulations with previous results give assurance that the simulations are done with realistic parameters. They also provide some clues to help estimate the energy resolution of the module.

The energy deposited in the $10 \times 10$ cm$^2$ regions covered by the light guides was separately measured in the simulations, in order to allow comparison with the experimental data. These checks are important because the energy resolution is sensitive to the amount of energy leakage from the calorimeter [16]. Both longitudinal (from the rear) and lateral (from the sides) leakage affects the energy resolution, and the lateral resolution affects the constant term in the energy resolution formula. The values obtained for the containment of the shower within the module (the energy leaking from the module) and the portion of the deposited energy that is outside the Front and Back regions (called Undetected in the table) are presented in Table 3.

Table 3: Leakage and undetectable portion of the deposited energy for positrons from Monte Carlo.

| Incident | without TOF | | with TOF | |
|---|---|---|---|---|
| Momentum (MeV/c) | Leakage (%) | Undetected (%) | Leakage (%) | Undetected (%) |
| 120 | 3.9 | 2.3 | 13.3 | 6.8 |
| 250 | 4.4 | 2.9 | 8.0 | 3.2 |
| 500 | 4.6 | 3.0 | 6.4 | 3.3 |
| 1000 | 5.2 | 3.5 | 6.0 | 3.7 |
| 2000 | 5.8 | 4.2 | 6.6 | 4.5 |

Without the TOF elements both the leakage and the umount of deposited but undetectable energy steadily increase with the energy of the incident positrons. With the TOF unit the high incident energies are comparable (they reach 6.6% and 4.5% respectively for the leakage and undetected fraction), but it is not so for the 250 MeV/c and especially for the 120 MeV/c samples. The values for 120 MeV/c with TOF are 13.3% for the leakage and 6.8% for the undetected fraction, which

is about three times higher than the without-TOF values. It will be shown that this affects the energy resolution significantly.

The reason for this higher leakage and undetected fraction is related to the variation in the position of the hit point on Module-1 was measured in the simulations and the fitted distribution showed about 1 cm (2 cm) standard deviation for 250 MeV/c (120 MeV/c) positrons. This spread influences the time measurements of each of the channels too. In time units, at 16 cm/ns effective speed of light, this would correspond to 62.5 ps and 125 ps, respectively. The Mean Timer eliminates this influence, but it should be noted that the spread occures not only along the long side of the module, but also along the 13 cm side (causing lateral leakage), and showers having unfavorable directions may produce very different timing characteristics of the scintillation light pulse.

## BCAL Beam Test with Photons at Hall-B

The prototype BCAL prototype module was tested in Hall B using a tagged photon beam in Fall 2006 [12]. As a reminder, the arrangement and naming of the BCAL readout segments (channels) for each end of the BCAL module is shown in Figure 4. The light guide coverage began flush with the front face of the module, and equally offset in the vertical direction. This left a thin strip of non-coverage along the top and bottom edges (each at 0.785 cm) of the Module as well as along its rear edge (0.34 cm). These values are accounted for in the Geant3 Monte Carlo simulations. The runs from the Fall 2006 beam test analyzed so far are listed in Table 4 and shown graphically in Figure 5.

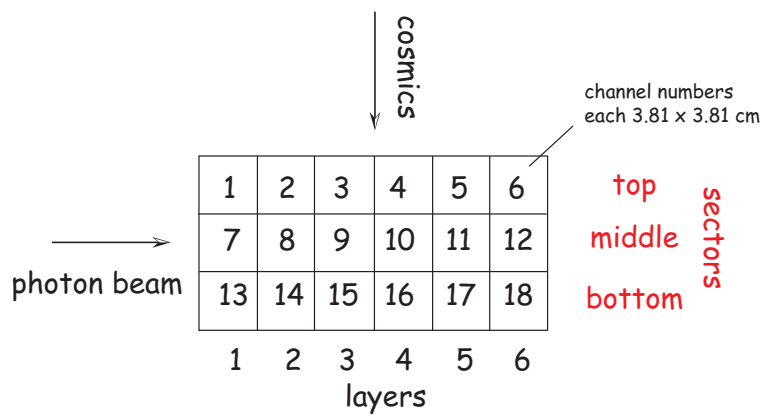


Figure 4: BCAL module readout arrangement at each end. The PMT's associated with layers 1 through 3 are readout using 18 XP2020 PMT's and layers 4 through 6 use Burle PMT's. The readout segments are each $3.81 \times 3.81$ cm$^2$.

The module was placed in the down stream alcove of Hall-B at Jefferson Lab. The use of a remote controlled cart allowed for the module to be rotated to various angles with respect to the photon beam. A hall access was needed to change the lateral position of the module with respect to the beam. The dimensions of the alcove limited the number of angle and position configuration: a length scan from $-100$ cm to $+25$ cm perpendicular to the beam was carried out along with multiple positions at shallow angles with respect to the beam.

Table 4: BCAL runs analyzed. For cosmic ray runs, the $z$-position refers to the position of the paddles along the BCAL module where $z = 0$ is the center and positive $z$ is towards the North end of the module. For photon beam runs the $z$-position refers to the impact point along the BCAL module at angle $\theta$. All the photon beam runs have been simulated under identical conditions.

| Run number | $z$-position (cm) | Angle | Comments |
|---|---|---|---|
| 2319 | 0 | 90° | Photon beam run, $y = +3$ cm |
| 2322 | 0 | 90° | Photon beam run, $y = +2$ cm |
| 2323 | 0 | 90° | Photon beam run, $y = +1$ cm |
| 2324 | 0 | 90° | Photon beam run, $y = -1$ cm |
| 2332 | 0 | 90° | Photon beam run, $y = -2$ cm |
| 2333 | 0 | 90° | Photon beam run, $y = -3$ cm |
| **2334** | 0 | 90° | Photon run, **golden run** |
| 2335 | −100 | 90° | Photon beam run |
| 2336 | −50 | 90° | Photon beam run |
| 2337 | 0 | 90° | Photon beam run, pre-radiator |
| 2338 | 0 | 90° | Photon beam run, pre-radiator |
| 2340 | 0 | 90° | Photon beam run, pre-radiator |
| 2363 | 0 | 40° | Photon beam run |
| 2367 | 0 | 10° | Photon beam run |
| 2368 | 0 | 20° | Photon beam run |
| 2369 | 0 | 30° | Photon beam run |
| 2393 | −100 | 10° | Photon beam run |
| 2398 | −190 | 10° | Photon beam run |
| 2458 | +150 | N/A | Cosmic ray run with XXX events |
| 2459 | +150 | N/A | Cosmic ray run with 46,593 events |
| 2460 | +150 | N/A | Cosmic ray run with 46,593 events |
| 2475 | −150 | N/A | Cosmic ray run with XXX events |
| 2476 | −150 | N/A | Cosmic ray run with 23,724 events |

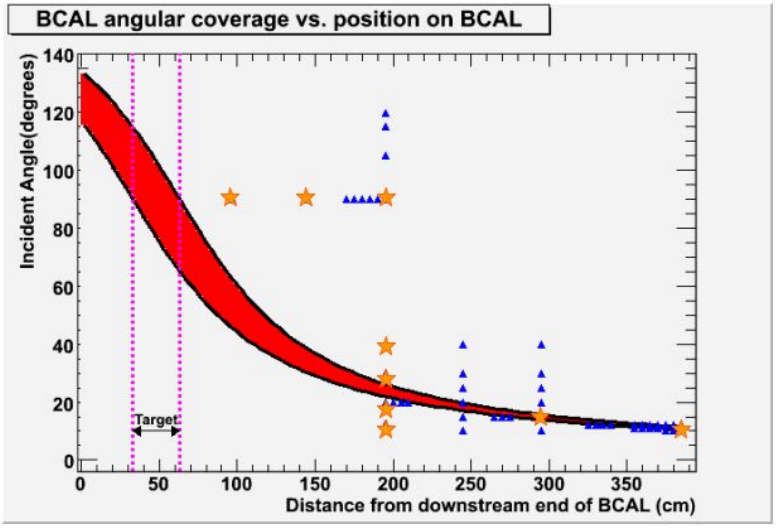


Figure 5: BCAL angular coverage versus position. The red band indicates the coverage during production runs, while the blue triangles show measurements taken during the beam test run in Hall-B, in September 2007. The orange stars display runs that have been analyzed, and this includes Monte Carlo simulations for the specific runs.

The bremsstrahlung photon beam in Hall B provided a spectrum of photons from 150 MeV up to 650 MeV produced by the 675 MeV electron beam from CEBAF incident on a radiator. The electron beam current was 1 nA. The scattered electrons are tagged and provide timing and momentum information for the photons. The tagger provides the momentum information from 384 individual scintillator paddles, called E-counters, with a photo-tube on each end. They are arranged so that they each cover constant momentum intervals of $0.003E_o$. Each counter optically overlaps its adjacent neighbour by 1/3 creating 767 individual photon energy bins providing an energy resolution of $0.001E_o$. The timing information is provided by 61 individual scintillator blocks, called T-counters, with phototubes attached at both ends. The T-counters are in two groups. The first 19 narrower counters cover 75% to 90% of the incident electron energy range and the remaining 42 counters cover the 20% to 75% range. The trigger is formed from the Master OR from the tagger of the T-counters and an OR signal from the North and South of the BCAL module. On average, the event rate was around 1 to 4 kHz for the duration of the beam test. The beam was collimated with a 2.6mm collimator giving a beam spot size on the BCAL module of 2cm in diameter.

Square light guides with a 45° mirrored surface channelled the light from the fibres to PMTs on the left and right end of the BCAL, labelled South and North respectively. Silicon sheets approximately 2.5 mm thick were used to interface the light guides with the BCAL and the PMTs. Everything was then enclosed in a steel box to maintain light-tightness. The first three layers were readout using XP2020 photomultiplier tubes because of their better timing characteristics and most of the energy is deposited in the first 12cm of the BCAL. The last three rows were readout using Burle 8575 tubes.

The bases for the PMTs were designed with dual BNC outputs on the anode. One signal was sent to a CAEN C 207 (equivalent leading edge) discriminator. An F1 TDC was used. The sum of the discriminator output was sent to a second discriminator and was required to reach a minimum threshold such that at least 4 PMTS each from the North and South end of the BCAL must fire. The effect of changing this threshold (number of PMTs that fire) will also be studied. The OR of the BCAL end sums AND the Master OR signal of the tagger established the trigger for the BCAL beam test.

## BCAL Energy Calibration and Resolution

The energy resolution is expressed in the form:

$$\frac{\sigma_E}{E} = \frac{a}{\sqrt{E(GeV)}} \oplus b \oplus \frac{c}{E(GeV)} \tag{2}$$

The $a/\sqrt{E}$ term indicates that sampling fluctuations and photoelectron statistics determine the resolution and will be refered to as the sampling term. The $1/\sqrt{E}$ dependence is expected from the fact that the fluctuations are proportional to the number of particle tracks, $n$, that cross the active material, where $n$ has a Poisson distribution with a variance $\sqrt{n}$. Since the energy of a shower is proportional to $n$, the sampling fluctuations contribution to the resolution $\sigma_E/E$ is $\propto 1/\sqrt{E}$. KLOE [17] determined the photon statistics from the light yield of their calorimeter to contribute $1.6\%/\sqrt{E}$ and determined it to be negligible. It is the sampling fluctuations that dominate the resolution. Since this is the case there should be little effect of z-position on the energy resolution as attenuation only affects the light yield at the module ends. This has been observed. Because the sampling frequency (how many layers or fibers the shower encounters) decreases with decreasing $sin(\theta)$, the sampling term of the resolution is degraded by a factor

$$\frac{\sigma_{samp}}{E} \propto \frac{1}{\sqrt{sin(\theta)}} \tag{3}$$

Also as one goes to angles less than 40° portions of the shower are lost outside of the module.

The constant term b is from mechanical imperfections, material defects, shower leakage, cell to cell calibration, uniformity of response and stability with time. At incident photon angles less than 40° shower leakage increases and will cause the floor term to increase. The noise term $c/E$ is from electronics noise and pileup in high rate environments. This term will dominate at the lower energies but has not been seen to contribute in the beam test as the rates were quite low and the signal to noise ratio was quite large.

### Energy Resolution from the TRIUMF 2005 Beam Test

The reason to use the Geometric Mean of the ADC signals is that the ADC channel is proportional to on the average 1/2 of the energy deposited by the shower $E_{left}$ or $E_{right}$ with a coefficient of

proportionality called the calibration constant $k$ and then this is multiplied by the attenuation for the respective z position:

$$ADC_{left} = k_{left} E_{left} \exp\left(-\frac{z}{\lambda}\right)$$

$$ADC_{right} = k_{right} E_{right} \exp\left(-\frac{L-z}{\lambda}\right)$$

which leads to

$$GM = \sqrt{ADC_{left} ADC_{right}} \propto \exp\left(-L/(2\lambda)\right) \tag{4}$$

where only the long component attenuation component is taken into account here. When used in the analysis, only points at a greater distance than 60 cm form the hit point to either end will be used, because at smaller distances the short component of the attenuation double-exponential contributes, and it is *not* canceled in the Geometric Mean. The energy resolution for each z for the respective incident energy and particle type was defined as $\sigma_{GM}/GM$. The results for positrons are shown in Figure 6.

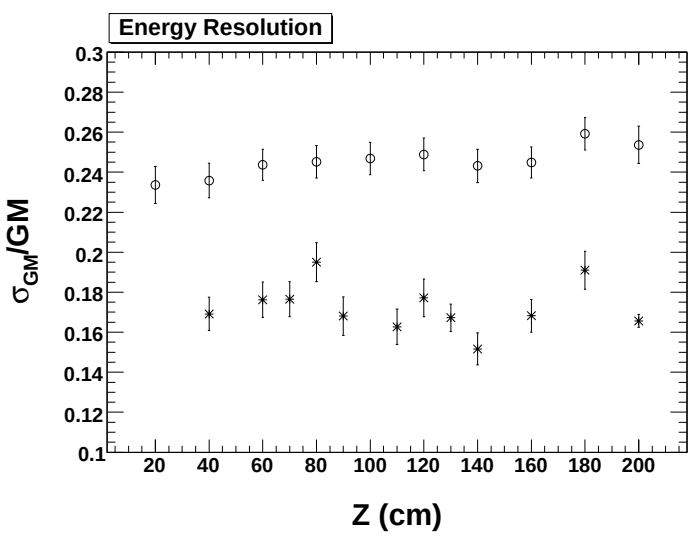


Figure 6: Ratio of the width of GM and GM itself (energy resolution) for positrons. The open circles (stars) correspond to the 120 MeV/c (250 MeV/c) data.

The values obtained by fitting the two incident energies were $24.6 \pm 0.3\%$ and $16.9 \pm 0.2\%$ for the 120 MeV/c and 250 MeV/c positrons. It should be stressed that that these values do not represent the intrinsic energy resolution of Module-1, but only the values obtained for the respective energies under the beam test conditions. The Monte Carlo simulations reported below provide details which will prove that the intrinsic energy resolution is actually much better.

It was verified that the Geometric Mean provides values for the width of the energy distribution equivalent to the sum of the calibrated energies in the left and the right sides within the error. The widths for the Geometric Mean and the sum of the energies for the midpoint $z = 200$ cm were $25.4 \pm 0.5\%$ and $26.8 \pm 0.5\%$, respectively. This means that the Geometric Mean and the sum of the Left and Right energies can be used interchangeably with little influence on the results.

The simulated dependence of the energy resolution on the incident positron momentum without

and with the TOF are shown in mathematical form below:

$$\frac{\sigma_{vis}}{E_{vis}} = \frac{(4.23 \pm 0.15)\,\%}{\sqrt{E_{inc}}} + (1.8 \pm 0.2)\,\%, \quad \frac{\sigma_{vis}}{E_{vis}} = \frac{(5.22 \pm 0.19)\,\%}{\sqrt{E_{inc}}} + (1.8 \pm 0.2)\,\% \tag{5}$$

The energy dependent term in the first equation sets the limits for the best achievable resolution with Module-1 for positrons. This number is slightly degraded due to lateral leakage. Under the beam test conditions there are two factors that will worsen the energy resolution: first, not all energy deposited in the fibers is detectable (the light guides cover only $10 \times 10cm^2$), and second, the presence of the TOF elements contributes to the leakage, thus deteriorating the resolution. Both these factors influence the sampling fraction fluctuations, and the energy resolution gets worse, as illustrated in the right panel of Figure **??**, where only the energy deposited in the Front plus Back volume is taken into account.

This plot shows that although the overall energy resolution does not change very much, the values for the lowest incident energies are quite different. For 120 MeV/c positrons the resolution is $(13.7 \pm 0.4)\%$ without the TOF and when the whole volume is taken into account, and $18.1 \pm 0.5$ with the TOF volume and when only the energy deposited in Front and Back is taken into account. For the 250 MeV/c positrons the numbers are $(10.3 \pm 0.3)\%$ and $(12.1 \pm 0.3)\%$, respectively. So adding the TOF to the experimental setup together with the effect of the only Front and Back volumes detection causes the energy resolution to get about 25% and 20% higher respectively. This effect of course decreases with the increase of the incident energy.

The next difficulty in the analysis was caused by the low number of events depositing energy in the Back region in the 120 MeV/c positron samples. The Monte Carlo simulations show that for this sample on the average about 1.3 MeV is deposited in the Back region, compared to 11.4 MeV in the Front region, per event. The deposited energy is of course attenuated, and events with low deposited energy do not pass the discriminator threshold, so in the experiment we see essentially no deposited energy in the Back region for most events. Therefore, only the Front portion can be reasonably compared to the Monte Carlo results.

Of course, as the incident energy gets higher, the energy deposited in the Back region gets larger, and the sampling fraction fluctuations in the Front region become larger. This is illustrated in Figure 7 where only the energy deposited in the Front region is plotted. As expected, the energy resolution gets better at first, but after 500 MeV/c it gets worse again, as a significant amount of the energy is no longer deposited in the Front region.

There are two important numbers here that can be directly compared to the experimental values. These two numbers are the values of the resolution for the 120 MeV/c and 250 MeV/c positron samples. The value for 120 MeV/c positrons from experiment is $24.6 \pm 0.3\%$ and from Monte Carlo is $22.1 \pm 0.7\%$. The value for 250 MeV/c positrons from experiment is $16.9 \pm 0.2\%$ and from Monte Carlo is $16.9 \pm 0.2\%$. The value from 250 MeV/c has an excellent agreement, with the number for 120 MeV/c from experiment being about 10% higher than the simulation.

There are three important remarks concerning this good agreement between experiment and Monte Carlo simulations. The first concerns the sampling fraction. Since the sampling fraction fluctuations are the most important factor for the energy resolution of sampling calorimeters, and assuming that GEANT does an excellent job in reproducing this (which is supported by the results of many

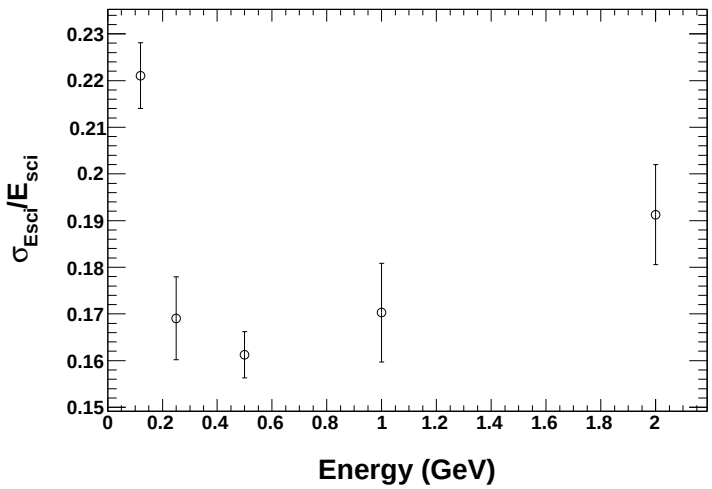


Figure 7: Simulated energy resolution for positrons for Front region only, with the TOF bars.

studies), it is reasonable to believe that there should not be any significant deviations between simulation and experiment. The second remark concerns the fact that the simulation takes into account for the averages even the most extreme events (e.g. positrons hitting the module near the edge, thus producing anomalous sampling and consequently influencing the resolution). Such events are likely to not be registered by the experiment because of the attenuation and threshold. To a certain extent, the experimental equipment cuts off the worst events. The third remark concerns the way the energy resolution was obtained from experiment. It is produced by the Geometric Mean of the ADC signals, plotted for all measured z-positions, with all the available statistics coming from consequtive (without changing the electronics parameters) runs, and then this is fitted with a horizontal straight line. So many factors (like the attenuation and consequently the fluctuations in the number of scintillation photons) are averaged out with high statistics in the experiment.

## Energy Resolution from the JLab 2006 Beam Tests

With the BCAL segmented into 18 cells on the North and South side this leaves us with 36 PMTs that each have their own applied high voltage, and thus 36 individual gains that must be balanced. Three different methods have been used to determine the relative gain of each of the cells.

**NOTE:** We should have a discussion here on how the gains were initially set and how ADC information is processed. Input from David will be needed. The issue of pedestal subtraction should be addressed.

## Calibration using Monte Carlo

In the first method the same Monte Carlo was used to determine the energy deposited in each cell. The photon energy spectra from the tagger was used as an input for the simulation. Fitting the peaks of each distribution allowed us to find an energy calibration for each cell. This method will

not be used further in this analysis as the beam test will be used to validate the Monte Carlo itself.

### Calibration using minimization

In the second method a minimization algortihm was used to adjust each of the gains to minimize the width of the parameter $D$ defined as

$$D = \frac{E_{BCAL} - E_{BEAM} * C}{E_{BEAM}} \tag{6}$$

where $E_{BCAL}$ is the reconstructed energy in the BCAL module and $E_{BEAM}$ is the energy measure in the tagger. C is a constant derived from Monte Carlo data to account for energy losses out the sides and back of the module as the goal is to reconstruct the deposited energy in the module and not the tagger energy. A value of $C = 0.95$ was found from a Monte Carlo simulation. The width of this distribution, $\sigma_D$, is also the energy resolution, $\sigma_E/E$.

The minimization technique accounts for the inter-PMT calibration. The overall calibration to relate ADC values to energy is determined by applying the inter-PMT calibration in determining the geometric mean of the sum of the North ADCs and the sum of the South ADCs and comparing this to the tagger energy as seen in Figure 8. The linear fit provides the slope and some offset most likely due to some minor error in the pedestal subtraction. In addition, one can see that the data points are not quite linear and fall below the fit at the higher energies. This is most likely due to increased leakage out of the module at higher energies. However, the linear fit takes care of most of the leakage in the reconstructed BCAL energy. Simulations show the reduction in photon energy sampling due to leakage. The losses scale nearly linearly above 200 MeV.

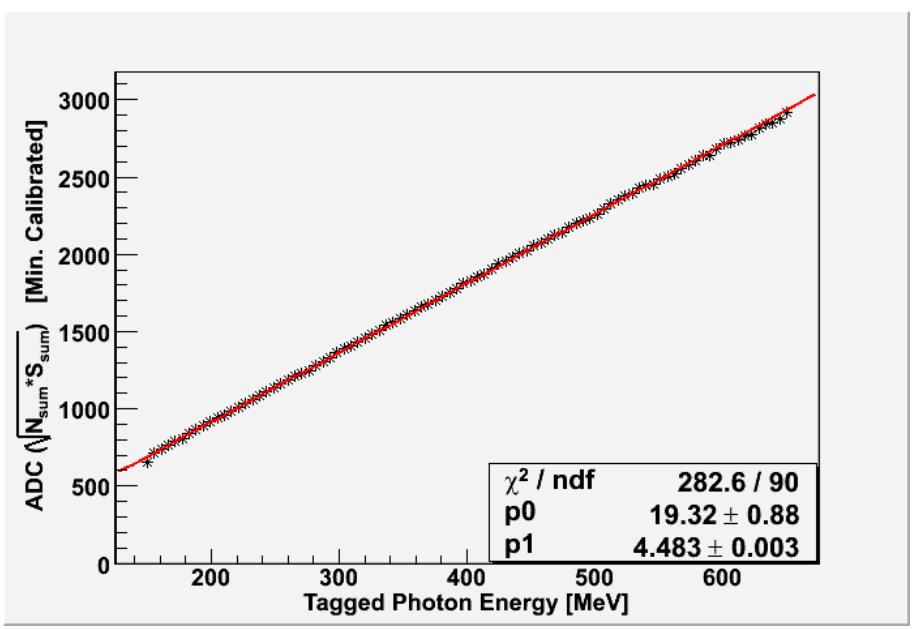


Figure 8: A plot of the ADC geometric mean (minimization calibration) vs. tagger energy with a linear fit.

## Calibration using cosmic ray information

The third method was to use cosmic ray data collected during the beam test to gain balance the 36 PMT's from the BCAL prototype module as described in [18] and are summarized here. The procedure described here was followed for runs 2476 and 2459 for which the comic trigger paddles were located at $z = -150$ cm and $z = +150$ cm respectively. First, for each of the 18 North/South cell combinations, twice the geometric mean of the two ADC's was formed if both ADC values were greater than zero; otherwise the two ADC's were simply added. The three-fold sum of these 18 cell sums associated with one of the 6 layers were then formed. Events were considered in which the layer with maximum ADC sum had more than 90% of the total ADC sum in the BCAL module. The three cells associated with that layer would be expected to have equal energy deposition from the the cosmic ray triggering that event. For each of these three cells, the ADC value associated with the PMT farther away from the trigger paddles was multiplied by $e^{2z/\lambda} = e^{300/257}$ to account for attenuation. The means of the resulting 36 ADC's (half of which were corrected) is shown in Figure 9 for runs 2476 and 2459. For the run with $z = +150$ cm, the South ADC's were corrected while for $z = -150$ cm, the North ADC's were corrected. The two runs track each other relatively closely. The inter-PMT calibration was determined applying a factor for each PMT to yield the same ADC mean, 334 in this case. Note that there are some outliers, channels 15, 16 and 17 for example. For photon running, these channels received little deposited energy.

The calibration constants obtained from this gain balancing technique and those obtained from minimizing the width of the $(E_{BCAL} - E_{beam})/E_{beam}$ distribution are shown in Figure 10 for North (left) and South (right) PMT's. The channels (7, 8 and 9) receiving the most energy from the photon showers are indicated by the dashed circles. Agreement here between the two methods is reasonably close.

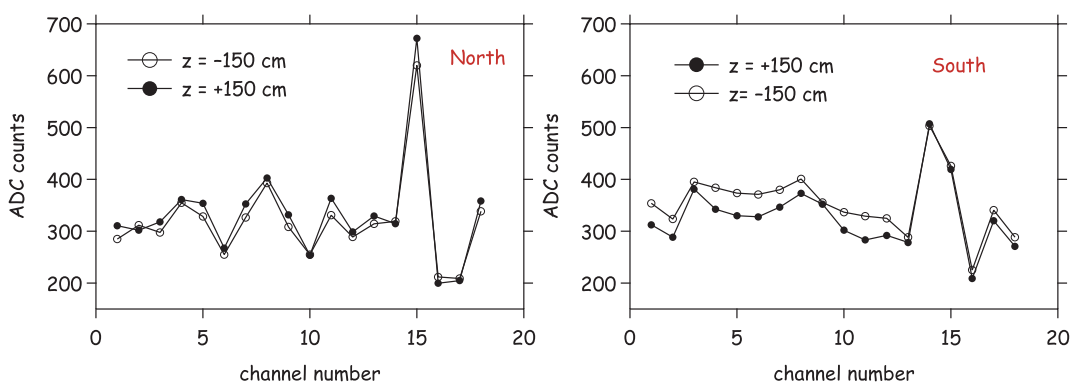


Figure 9: Means of the ADC's associated with the 36 BCAL PMT's before gain balancing, for events in which a layer contains 90% of the energy in a cosmic ray event, for runs 2476 and 2459. For a given run, the ADC from the PMT further away from the cosmic trigger paddle counters was corrected to account for the loss due to attenuation. More details are given in the text.

In Figure 10 we show the calibration constants obtained from gain balancing and those obtained from minimizing the width of the $(E_{BCAL} - E_{beam})/E_{beam}$ distribution for North (left) and South (right) PMT's. Note that the channels needing the large corrections for gain balancing of cosmic data are those channels which have little photon shower deposited in them.

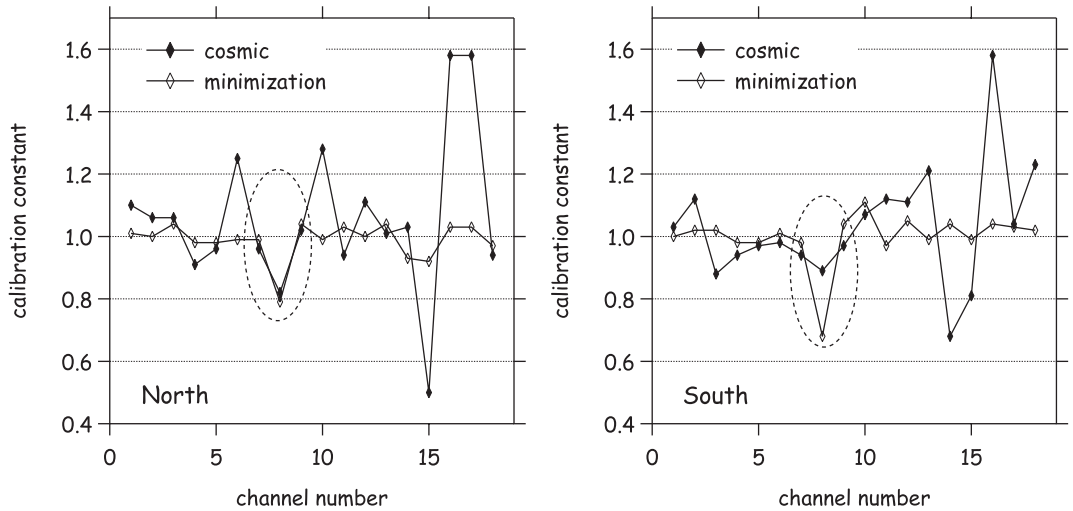


Figure 10: The calibration constants obtained from gain balancing and those obtained from minimizing the width of the $(E_{BCAL} - E_{beam})/E_{beam}$ distribution for North (left) and South (right) PMT's. The channels (7, 8 and 9) receiving the most energy from the photon showers are indicated by the dashed circles.

The calibration constants obtained from this balancing technique were then applied to the photon run 2334 where the beam was normally incident at the center of the BCAL module. The $(E_{BCAL} - E_{beam})/E_{beam}$ distribution for bins in $E_{beam}$ were fit to a Gaussian to obtain $\sigma_E/E$. The results with and without inter-channel calibration are shown in Figure 11. The curves are a result of a fit to the parameterization $\sigma_E/E = a\sqrt{E} \oplus b$ where $E$ is in GeV. The fit yields $a = 5.7 \pm 0.3$ and $b = 5.3 \pm 0.5$ percent for data without gain balancing and $a = 5.5 \pm 0.2$ and $b = 2.9 \pm 0.7$ with gain balancing. Also shown are the results of using the calibration constants resulting from the minimization technique and the resulting fit parameters are $a = 5.5 \pm 0.2$ and $b = 2.1 \pm 1.0$.

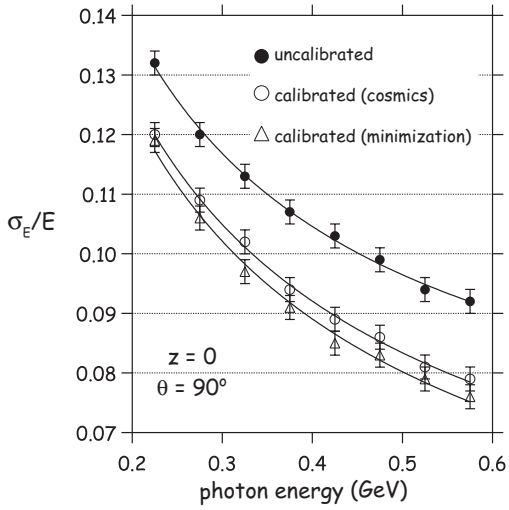


Figure 11: $(E_{beam} - E_{BCAL})/E_{beam} = \sigma_E/E$ as a function of photon energy for Run 2334 for no calibration (filled circle), calibration using cosmics (open circles) and calibration using the minimization technique. The curves are the result of fits to a resolution function of the form $a/\sqrt{E} \oplus b$. Fit parameters are given in the text.

### Energy resolution as a function of position and angle

The energy resolution for the two methods and for different angles is shown in Figures 12 and 13. In Figure 14 we show the resolution as a function of beam energy for photon runs at normal incidence for $z = 0$ (run 2334), $z = -50$ (run 2336) and $z = -150$ (run 2335) without (left) and with (right) gain balancing. The resulting values of the fit parameters $a$ and $b$ are given in Table 5.

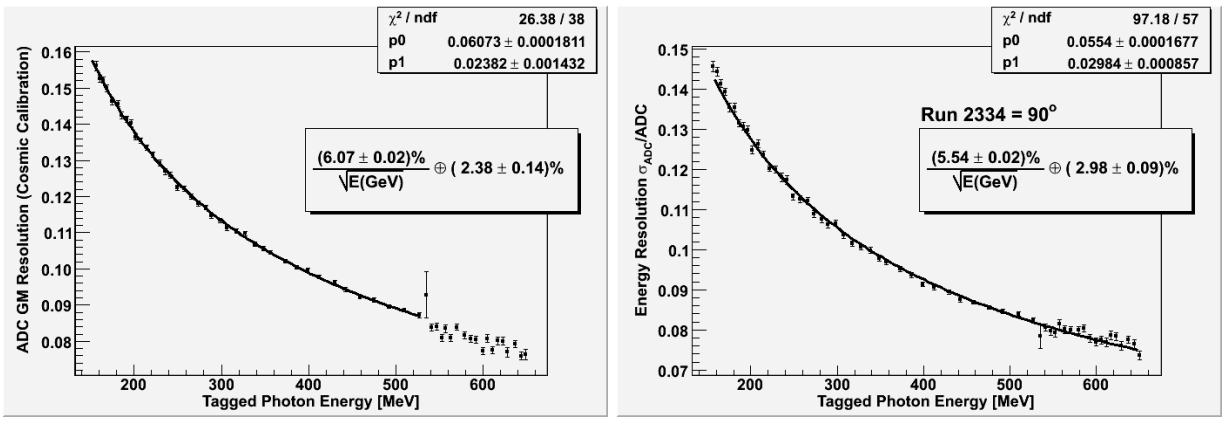


Figure 12: The energy resolution using cosmic ray calibration for each cell on the left, and using the minimisation algorithm calibration on the right.

Table 5: The fit parameters $a$ and $b$ obtained for the resolution function $\sigma_E/E = a/\sqrt{E} \oplus b$

| z (cm) | incident $\theta$ | Calibration | a (%) | b (%) |
|---|---|---|---|---|
| 0 | 90° | None | $5.7 \pm 0.3$ | $5.3 \pm 0.5$ |
| 0 | 90° | Cosmics | $5.5 \pm 0.2$ | $2.9 \pm 0.7$ |
| 0 | 90° | Minimization | $5.5 \pm 0.2$ | $2.1 \pm 1.0$ |
| $-50$ | 90° | None | $5.6 \pm 0.2$ | $5.3 \pm 0.5$ |
| $-100$ | 90° | None | $5.6 \pm 0.2$ | $5.3 \pm 0.5$ |
| 0 | 40° | None | $5.9 \pm 0.2$ | $3.8 \pm 0.6$ |
| $-50$ | 90° | Cosmics | $5.6 \pm 0.2$ | $2.8 \pm 0.8$ |
| $-100$ | 90° | Cosmics | $5.5 \pm 0.1$ | $2.5 \pm 0.9$ |
| 0 | 40° | Cosmics | $5.8 \pm 0.2$ | $1.7 \pm 1.3$ |

### Converter Runs

This analysis was reported in detail in reference [19]. The highlights are reproduced here. In the Pb-converter runs there is a high percentage of events that have no energy in the tagger (i.e, Ephoton=0). To clean up the sample, the following cuts were applied:

- Only one reconstructed photon in the tagger (Nphoton=1).
- Energy of the photon non-zero (Ephoton>150 MeV).

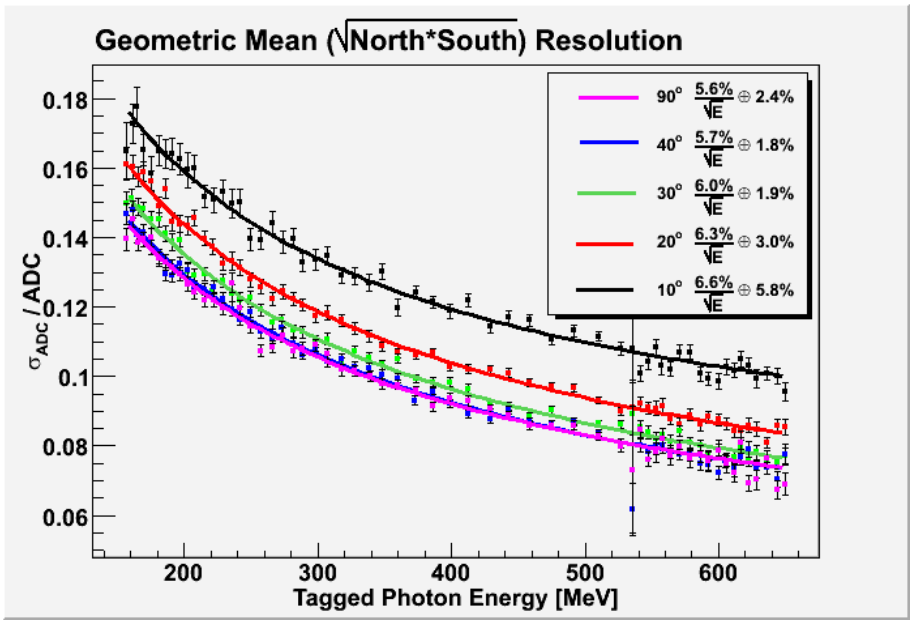


Figure 13: The energy resolution for different angles.

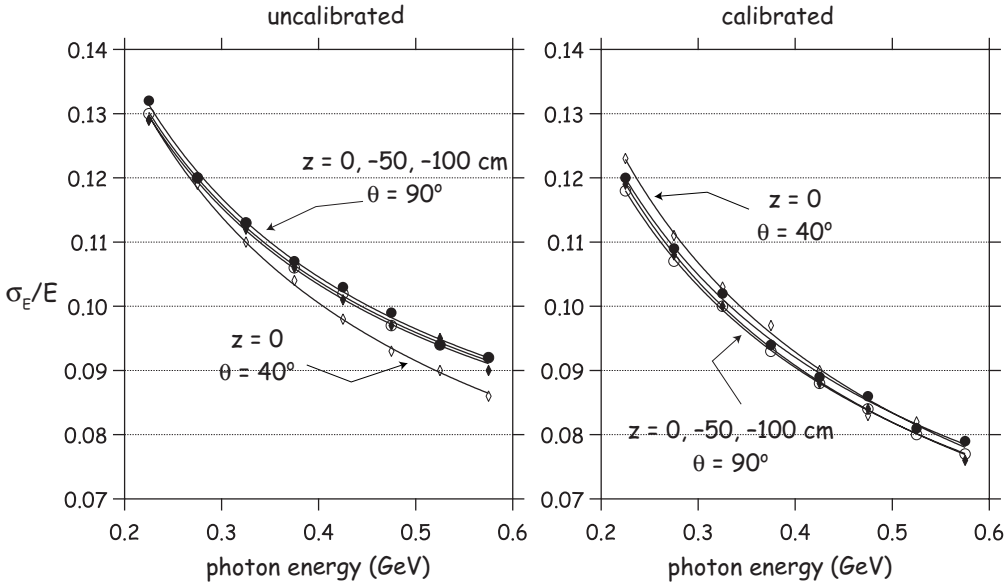


Figure 14: The resolution as a function of beam energy, along with fits, for photon runs at normal incidence for $z = 0$ (run 2334), $z = -50$ (run 2336) and $z = -150$ (run 2335) without (left) and with (right) gain balancing. The resulting values of the fit parameters $a$ and $b$ are given in Table 5.

- Timing of the beam around the peak of 600nsec (580<tphoton<610nsec).
- Ntdctrig$\geq$ 8.
- The veto contributed negligible rejection and was not used.

After the above cuts about 200,000 events were left in each run allowing a division into energy slices with minimum statistics of 15,000/slice. Runs 2334 (without converter), 2337 (1.5 mm Pb), 2338 (3 mm Pb) and 2340 (with 4 mm converter) were analyzed, using the adjusted gains from the resolution minimization method [20]. The different runs didnt show much more than 1% variation on the gains, so the same gains were used for all runs. The ADC-to-energy calibration factors were determined to be 0.2191 for Run 2334 , 0.2191 for Run 2337, 0.2194 for Run 2338 and 0.2208 for Run 2340.

The resolutions as a function of energy are shown on Figure 15, for the three different converter runs compared always to the non-converter run (shown in red). The three figures clearly show a deterioration of the energy resolution as the thickness of the converter increases. In order to quantify this, the energy dependence was fit to determine the two coefficients. The results are shown in Figure 16 as a function of Pb thickness. The top plots show a 6% deterioration of the energy resolution with pre-radiator thickness.

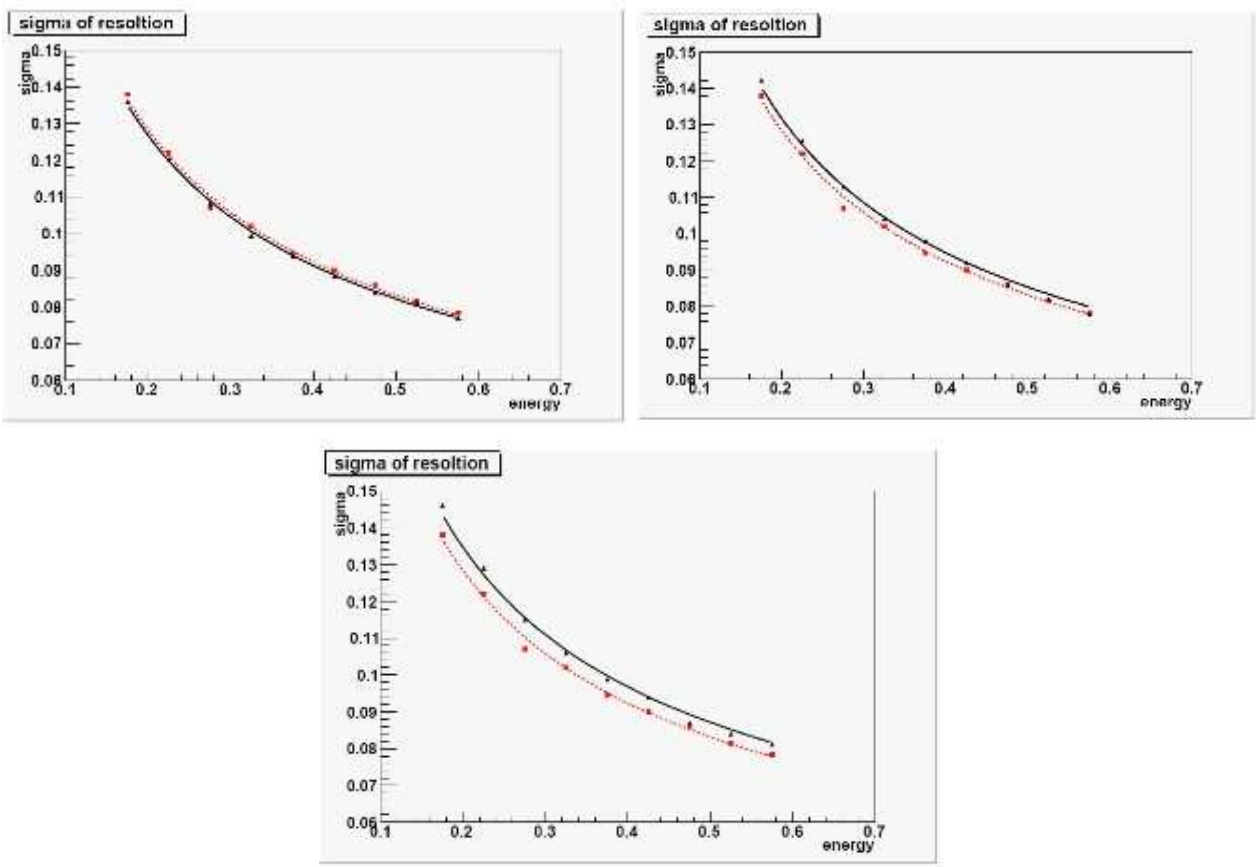


Figure 15: Sigma/energy resolution for Run 2334 (red) and runs 2337, 2338 and 2340 (black) as a function of energy.

Differences in the lateral and longitudinal shower profiles were examined, although the coarse segmentation of the read-out (every $2.8X_0$) does not allow for a precise analysis. Indeed the lateral shower profiles for every of the three rows (summing the 6 PMs in each row), do not show any appreciable differences. In any case the RM of the BCAL is of the order of 4cm, namely one read-out subdivision. On the other hand, the longitudinal shower profiles, which compare the energy

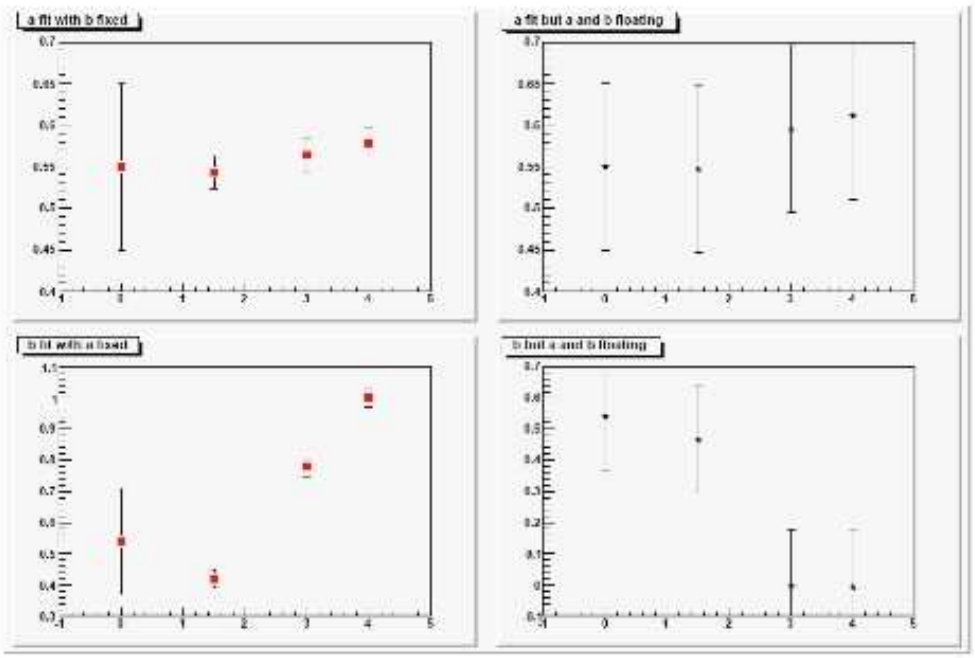


Figure 16: The $a$ and $b$ coefficients of the energy resolution fit, $a/\sqrt{E}+b$, as a function of the Pb thickness in mm. On the top left plot $a$ is shown keeping $b$ fixed, on top right $a$ is shown for $b$ free and in the lower plots $b$ is shown keeping $a$ fixed (doesnt make much sense) and $b$ having $a$ free.

deposited per row for the six columns (summing the 3 PMs in each column), are different for runs 2334(Red)/2338(blue) and 2334/2340(black) respectively. For the photons, the shower maximum is deeper and therefore less energy ($\simeq$23%) is deposited in the first column, whereas for the converter runs-where we have a mixture of electrons and photons- the shower starts earlier its development and more energy is deposited in the first column ($\simeq$30%).

The longitudinal development of an electromagnetic cascade depends on the high-energy part of the cascade, and therefore scales with the radiation length in the material. The mean longitudinal profile of the energy deposition of an electromagnetic cascade is expressed as:

$$\frac{dE}{dt} = E_0 b \frac{(bt)^{a-1} e^{-bt}}{\Gamma(a)} \tag{7}$$

where $E_0$ is the incident particle energy, $t = x/X_0$ is the depth inside the material, and $a$ and $b$ are parameters related to the nature of the incident particle ($e^{\pm}$ or $\gamma$). The values of $X_0$=1.45 cm and $E_c r$=8.36 MeV were used [11]. This formula doesnt apply well when the energy is below 300MeV, so Ephoton>300MeV was required as a condition before the fit. During the Jlab running $\bar{E_0}$=355 MeV. These values result in $a = 3.13$ for gammas and $a = 2.63$ for electrons. Therefore one expects that above formula will fit the distribution of photon runs with $a = 3.13$ and the distributions of pre-radiator runs will be fit with a linear combination of formula with $a = 3.13$ and another with $a = 2.63$. Indeed from the formula $I = I_0(1 - e^{-7t/9X_0})$ with t=3 and 4 mm, 36% and 43% of the photons have converted into electrons respectively.

The longitudinal profile fit for Run 2334 was left free and the result was $a = 3.55 \pm 0.03$ (whereas the value predicted by the formula is $a = 3.20$ at an average energy of 410 MeV). For the other three runs $a$ was kept fixed, and the shower profiles were fit to a linear combination of gamma and electron profiles: $f_1\times$gamma profile $+f_2\times$electron profile (where the electron profile has $a_e = a_\gamma - 1$). All fits leave the normalization of the electron component free in order to determine the % of converted gammas. The values determined by the fits are shown on the Table 6, and are not in good agreement to the predictions of the $I/I_0$ formula of 66% and 57% respectively.

Table 6: Percent of converted photons as derived from the analyzed shower profile and the analytical calculations.

| Pb Thickness (mm) | % of converted $\gamma$ (shower profile) | % of converted $\gamma$ (analytical) |
|---|---|---|
| 0 | 0 | 0 |
| 1.5 | 25 | 19 |
| 3.0 | 56 | 34 |
| 4.0 | 76 | 43 |

Adjusting the individual gains of each PM has the effect of lowering (by a factor of two at least) the constant term of the energy resolution. Nevertheless the fact that the PMs with the max energy deposition are considerably lowered in both read-out sides, looks to be an unnatural choice. The small adjustments of gains in order to improve the resolution are necessary but it is no coincidence that the central PMs need to be turned-off "by hand" by 30%. This influences considerably the lateral profile and probably results to an artificially small constant term. The effect of the addition of the converter results in a deterioration of the $1/\sqrt{E}$ term of the resolution by at most 10% (for the 4mm Pb thickness). The fits of the shower profiles give percentages that are not far from the analytical values. This is probably due to the coarse segmentation of the calorimeter.

## Validation Simulations

This section should include comparison of energy deposition profiles from data, simulations and analytical expectations. Preliminary results will be shown at the Calorimetry Workshop (Jefferson Lab, July 26-28, 2007).

## Sampling fraction fluctuations

In a sampling calorimeter, such as the BCAL, the energy deposited in the active medium (scintillating fibers) fluctuates event by event since the active layers are interleaved with Pb layers. These are the above mentioned sampling fluctuations and are the largest contribution to the energy resolution. They depend on variations of the number of charged particles, $N_{ch}$, which cross the scintillating fibers:

$$N_{ch} \sim \frac{E_0}{t} \tag{8}$$

where $t$ is the thickness of the inactive layers in $X_0$ units. For statistically independent cRossi:1952ngs of the active layers, the contribution to $\sigma(E)/E$ due to the sampling fluctuations is given by [21]:

$$\frac{\sigma(E)}{E} \sim \frac{1}{N_{ch}} \sim \sqrt{\frac{t}{E_0}} \tag{9}$$

Clearly, less absorber and more scintillating fiber thickness (i.e. larger *sampling fraction*) improves the energy resolution, at the expense of 'stopping power' (total thickness in number of radiation lengths) of the calorimeter due to the low detector density. For a sampling calorimeter to match the energy resolution of a homogeneous one, inactive thickness of a few percent is needed, which is impractical. Moreover, a low calorimeter density implies that the showers need more space to develop in all directions thus resulting in overlapping clusters and impeding the particle identification process, and it also results in an increase of the $e/h$ value of the calorimeter which degrades its 'compensation' capability towards detection of hadrons. A second way of reducing sampling fluctuations is to increase the *sampling frequency*, which is depends on the number of independent sampling layers for a fixed sampling fraction. This can be achieved by reducing the scintillating fiber diameter while introducing more layers to keep the sampling fraction constant.

In order to understand these two effects on the energy resolution, recall that the energy of a showering photon or electron is primarily deposited in the inactive material (Pb for the BCAL) via a very large number of 'soft' electrons [22]. These secondary electrons have average energies much lower than the critical energy of the material and an effective range that is much less than the inter-layer distance. For the BCAL, the atomic number of the inactive material ($Z = 82$) is much larger than that of the active material ($Z = 5.615$) so the overwhelming majority of these soft electrons are produced and absorbed in the inactive material, because of the $Z$-dependence of Compton scattering and the photoelectric effect [16].

Most of these electrons will not contribute to the calorimeter's signal; the sampling fluctuations come from those that *do* contribute. This number can be increased by increasing the total surface of the boundary between active and inactive layers, which can be achieved by either increasing the sampling fraction or sampling frequency. However, such increases result in modest gains in resolution: for example, reducing the fiber diameter from $1.0\,mm$ to $0.5\,mm$ results in four times as many fibers per unit volume, yet the energy resolution improves only by a factor of $\sqrt{2}$. In other words, the resolution scales with the fourth root of the number of fibers. This has significant implications in cost and manpower for handling and construction.

The sampling fraction is indeed an important parameter of sampling calorimeters, and can be expressed as:

$$f_{samp} = \frac{E_{mip}(active)}{E_{mip}(active) + E_{mip}(inactive)} \tag{10}$$

It should be noted that this quantity impacts the noise term of the energy resolution [23], a point that will be discussed further in Section 6.1.3. For a fixed number of $X_0$ in the BCAL, the stochastic term of the energy resolution is approximately equal to $6\sqrt{t/f}$, where $t$ is the inactive plate thickness (0.089) and $f$ the sampling fraction (0.12), resulting in $a \simeq 5\%$ for the BCAL [24]. The contribution of the sampling fluctuations has been simulated and shown in Figure .

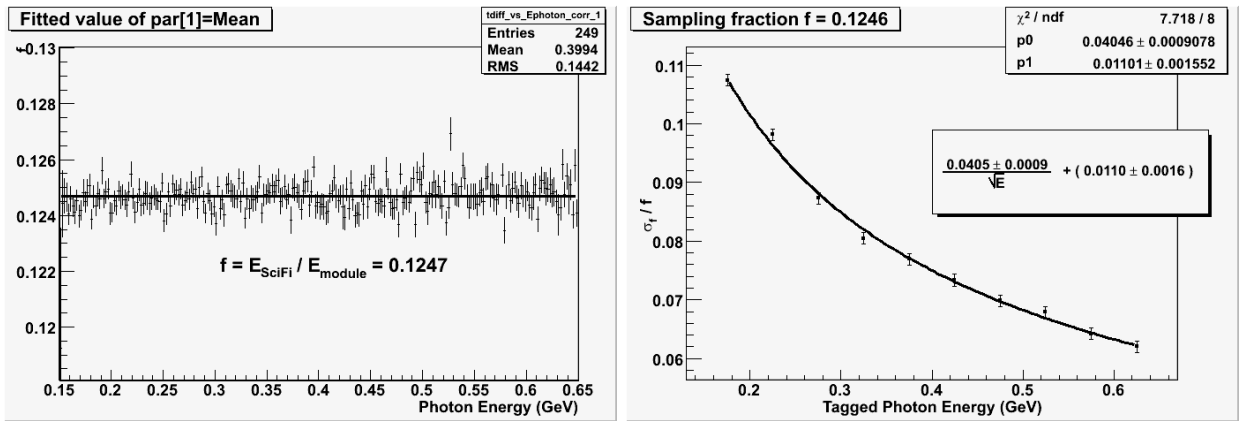


Figure 17: Simulation of the BCAL sampling fraction and its resolution as a function of tagged photon energy, corresponding to the Fall 2006 Beam Test at Hall-B/Jefferson Lab.

# BCAL Timing Resolution

## Timing Resolution from TRIUMF 2005 Beam Test

A major contribution to the time resolution is the size of the beam spot. Since all the incident particles do not hit the face of the module at the same spot, the times for reaching the left and right side will be different on an event by event basis, adding to the width of the time distribution. As it will be shown below, the point of hit has a width of about 2 cm (corresponding to about 125 ps) for the 120 MeV/c positrons, and about 1 cm (corresponding to about 62.5 ps) for the 250 MeV/c positrons. This contribution is removed in the Mean Timer. Furthermore, the number of photons that reach each PMT, fluctuate from event to event - depending on the distribution of the initial angles of the created photons and their attenuation. Since roughly half the scintillation photons will travel Left and half will travel Right, assuming ideal other conditions, the widths of the time distributions of MT and Left (or Right) time will be related as $\sigma_{MT} = \sigma_{left}/\sqrt{2}$.

The width of the Mean Timer distribution represents the time resolution at the respective energy. For both positron energies the width was fitted with a horizontal straight line, and the results obtained are $\sigma_{MT} = 337\pm$ ps and $\sigma_{MT} = 232 \pm 7$ ps for the 120 MeV/c and 250 MeV/c positrons, respectively. This can be regarded as a first approximation for the time resolution at the respective energies, but there are more factors to take into account.

## Processing of TDC information from JLab 2006 Beam Test

**NOTE:** Additional information may be required here from David and Simon.

For information on the method of extracting the intrinsic timing resolution from the BCAL the reader is directed to reference [25]. Because leading edge discriminators were used, the timing had a dependence on pulse height which required a time walk correction. A $p0/\sqrt{ADC} + p1$ fit was

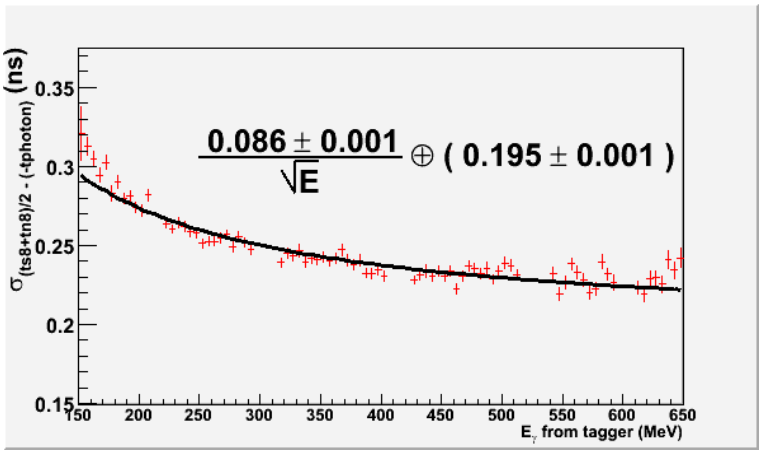


Figure 18: Timing resolution from cell8.

applied to the ADC versus TDC plots for North and South cells 7,8,9 and 10 so far.

### Time resolution from photon data

Distributions of the cell mean timer over the entire tagger energy spectrum were formed, for several cells. The timing from the tagger, tphoton, has been used as the reference time for the BCAL which has a contribution to the constant term in the resolution of 113 ps . Likewise, the distribution for the time difference of South minus North for various cells were also examined. A plot of the timing resolution of cell 8 can be seen in Figure 18. The width of the photon beam (2 cm) will contribute 123 ps to the time difference resolution (not shown in this note) where the speed of light in the BCAL is measured to be 16.2 cm/ns. The width of the em shower will also contribute to the time difference resolution.

Subtracting the contribution of the tagger to the resolution, 113 ps, we are left with a resolution for the mean timer for cells 8 and, $\sigma((ts_i + tn_i)/2 - (t_{tagger}))$, equal to

$$\sigma_{t8_{MT}} = \frac{86ps}{\sqrt{E(GeV)}} \oplus 159ps, \quad \sigma_{t7_{MT}} = \frac{61ps}{\sqrt{E(GeV)}} \oplus 176ps \tag{11}$$

where $\oplus$ indicates addition in quadrature and $t_{tagger}$ is the reference time from the tagger. Since this is the result for the sum of 2 detectors the resolution for reading out one end will be $\sigma_{t7_{MT}} * \sqrt{2}$. The resolutions for one end of cell 8 and cell 7 respectively are then

$$\sigma_{t8} = \frac{122ps}{\sqrt{E(GeV)}} \oplus 225ps, \quad ; \sigma_{t7} = \frac{86ps}{\sqrt{E(GeV)}} \oplus 249ps \tag{12}$$

Weighting the time of each cell by $1/\sigma_i^2$ the time for a cluster is equal to

$$t_{cl} = \frac{\sum_i \frac{t_{MT}(i)}{\sigma^2_{MT}(i)}}{\sum_i \frac{1}{\sigma^2_{MT}(i)}} \tag{13}$$

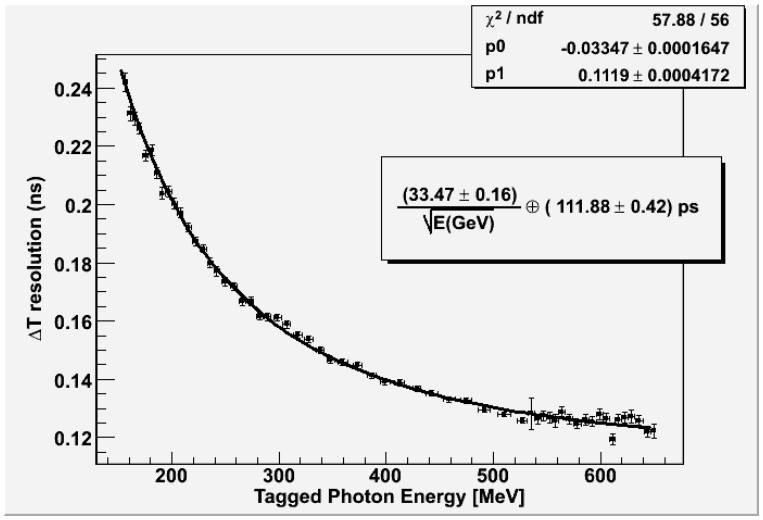


Figure 19: The time difference resolution, $\sigma_{\Delta T}$, as a function of energy.

where there are i cells in the cluster. For now, just adding cells 7 and 8 (4 PMTs) together and subtracting the contribution from the tagger then yields a resolution of

$$\sigma_{t7\&8} = \frac{60ps}{\sqrt{E(GeV)}} \oplus 149ps \tag{14}$$

Care must be exercised when performing the time walk corrections due to the fact that the t-counters of the tagger corresponded to a given energy range as they are physically positioned in front of a set of e-counters. When using the tagger as a reference for walk corrections, there resulted an energy dependence on the time which was included in the correction. Secondly, ADC cuts influence the energy resolution and should be applied with caution.

A cluster is defined as the energy weighted sum of the times of each cell expressed as

$$\bar{T} = \frac{1}{2}\frac{\sum_i t'_{N,i}E_{N,i} + t'_{S,i}E_{S,i}}{\sum_i(E_{N,i} + E_{S,i})} \tag{15}$$

$$\Delta T = \frac{1}{2}\frac{\sum_i t_{N,i}E_{N,i} - t_{S,i}E_{S,i}}{\sum_i(E_{N,i} + E_{S,i})} \tag{16}$$

The $t'$ indicates that the time is referenced with another time signal, usually the tagger. For effeciency only cells 7, 8, 9 and 10 were included in the cluster as they contain 85-90% of the shower energy. To be included in the cluster it was required that the North and South end of the cell both have ADC signals greater than 5 channels. This corresponds to ∼1 MeV of energy deposited in the BCAL or $\tilde{0}$.12 MeV deposited in the fibers. The mean time of the cluster, $\bar{T}$ or the time difference, $\Delta T$, was then calculated and the sigma of the distributions then found. The time difference resolution is seen in Figure 19.

### Time resolution from cosmic ray data

For details the reader is directed to reference [26]. To further study the time resolution, we look at cosmics which transverse the BCAL. To make sure that we do, we have plotted the correlation of PHs of blocks 3, 9 and 15. The plots for channels 15 and 9 show a clear correlation. Large PHs of one correspond to large PH of the other. So we decided to select events which have PH>100 in both blocks and calculate the differences of the average (North+South)/2 walk-corrected TDC values for all the three combinations.

The time difference between cells 15 and 3 was found as the best of three possible and the time resolution was extracted from this pair. The expected time for light to travel the distance for vertical events (center to center 8 cm) is 510 psec. For inclined events the distance can be as large as 13cm diagonally across- so the time comes out to 840 psec. On the sigma of the time difference, one has to add the jitter due to the width of the trigger counters ± 4.5 cm width which is another 290 psec. So taking the time jiiter off (in quadrature) one ends up with a time resolution of about 520 ns Besides, the calculation of this top-bottom time difference, for straight through tracks, should be independent of the paddle position. This is confirmed by analyzing it as a function of z: the slope is zero within errors and the average value of the time difference is 1.5 nsec.

The following analysis is courtesy of Elton Smith. Starting from the measured $\sigma(15WC - 3WC) =$ 0.65 ns and assuming the same time resolution for both 15 and 3, we get $\sigma_{measured}(15WC) = \sigma(3WC) = \sigma(15WC - 3WC)/\sqrt{2} = 0.46$ ns. This would correspond to the time resolution for one cell with an average energy deposition given by a cosmic-ray traversing one cell. The equivalent energy for minimum ionizing in the direction of the beam is about 170 MeV, and vertically the desposited energy is 2/3(170) = 113 MeV. The energy in one cell is 113MeV/3≃40 MeV. Now there are corrections to this value due to fluctuations not associated with the timing measurement itself: 1) size of the source (although this should partially cancell out when taking the difference between cells 15 and 3 and 2) path length variations in the cosmic-ray tracks between 15 and 3. Let's take each one of these in turn (as my naive analysis differs from your numbers):

- Size of the source. The paddles have a width of 9 cm, so a uniform distribution over 9 cm gives a $\sigma$ = 9 cm/sqrt(12) = 2.6 cm. Using the Athens number for the velocity in the barrel of 15.5 cm/ns, this contribution gives 2.6cm/15.5cm/ns = $\sigma_{source}$ = 167 ps.
- Path length variations. Here, we take the numbers of 8 cm for direct path and 13 cm max for inclined paths (if I understand them correctly). I could take a naive estimation for the sigma as (13-8 cm)/$\sqrt{12}$ = 1.44 cm as above. Alternatively one can compute the sigma assuming a uniform distribution of cosmic rays in phase space dN/dcosthe = constant (this actually overestimates the variation): $\sigma^2_{path} = \bar{p^2} - \bar{p}^2$, where p = 8 cm/cos($\theta$). The averages give: $\sigma_{path} = 8cm\sqrt{1.613 - 1.582} = 8cm(0.176) = 1.4cm$, similar to the above number.

For cosmic rays we can assume 30 cm/ns (velocity of light). Therefore, we get $\sigma_{path}$ =1.4cm/30cm/ns = 47 ps. In summary, we conclude the following: $\sigma(15WC) = \sigma_{measured}(15WC) - 167 - 47$ (in quadrature), which gives $\sigma(15WC) = 426$ ps. In order to compare with the photon analysis, we can plug in 40 MeV into his parametrization $\sigma_t = 64/\sqrt{0.040} + 134ps = 454$ ps. This is in fairly good agreement if this interpretation is correct.

## Time and Position resolution as a function of position and angle

**NOTE:** This has not been done yet. This discussion will be based on time difference information.

## Effective Speed of Light in Fibers

### Charged Particle Beam Test at TRIUMF

The effective speed of light can be extracted from the slope of the plot of the time of arrival at each PMT versus z, or from the slope of the plot of the Time Difference versus z (in this case the slope will be twice the effective speed of light). One reason to use the Time Difference for the effective speed of light is, for example, that when z is not 200 cm (the midpoint for the TRIUMF tests), the light that travels to the more distant PMT will be attenuated more and this will happen with higher probability to the photons emitted at angles close to the angle of total internal reflection and with lower probability with the photons that are emitted at angles closer to the fiber axis. This qualitative argument shows that we can expect the more distant PMT to produce a signal corresponding to a slightly higher effective speed of light. The Time Difference, on the other hand, removes this effect by averaging the final values of the times measured by the Left and the Right TDCs.

The plot of the Time Difference versus z yielded an effective speed of light of $c_{eff}(TD) = 16.2 \pm 0.4$ cm/ns. This is in good correspondence with the previously measured value using cosmic rays at the Regina detector lab. The values from the Left and Right TDCs are 15.6 ± 0.4 cm/ns and 16.8 ± 0.6 cm/ns, respectively. As expected, the Left TDC (the left end is always either closer or at the same distance as the right end), has a slightly smaller value for the effective speed of light.

Similar results are obtained from the 250 MeV/c positrons. When the energy of the incident particles increases, first the spread of the hit point is smaller, and second we expect higher number of scintillation photons to be produced, thus decreasing the fluctuations and the widths of the distributions respectively, which is reflected in the smaller deviations of the values for this case: 15.9 ± 0.5 cm/ns for Left, 15.4 ± 0.5 cm/ns for Right, and 15.7 ± 0.5 cm/ns for the Time Difference.

Of course, calculating the Time Difference, but on an event by event basis, has another, more important reason - the position of the shower (determined by the entry point of the incident particle) can be only estimated by the Time Difference, so it is the timing quantity directly related to the spatial resolution in z. It will be used in this respect in the reconstruction of the observed events.

### Cosmic Runs at Regina

In 2001 cosmic tests with bundled fibers (i.e not embedded in a lead matrix) gave $v_{eff} = 19.1$ cm/ns. See GlueX-doc-50 for further details.

**Cosmic Runs at Hall-B**

This analysis was reported in detail in reference [26]. The highlights are reproduced here.

Cosmic ray runs 2458, 2459, 2475 and 2476 were used in this analysis (see Table 4). The dimensions of the paddle counters were 23cm length and 9cm width and they were placed above (1") and below (2") the BCAL, their small dimension along with the long dimension of the calorimeter. [Alex: a bit more here on the setup from one of your notes]...

The TDCs for all 36 PMT's were examined. If one looks at individual TDC's a multi-peak behaviour emerges. However, if one takes one PMT as a reference any block (example North 3) and subtracts it from both all other PMT's, then the different peaks cancel out and there remains only one peak. We have also investigated the energy deposition for each of all peaks. The average PH does not support the hypothesis that different peaks belong to different energy depositions.

The speed of light was determined by taking left minus right differences for all the four different paddle positions given in table I and for three different channels. The channels which belong to layer 3 (middle of the BCAL), were used to this end. These are the channels 3, 9 and 15. From the time differences as a function of z we calculated speed of light for the three different channels and results are shown on Table 7. It comes out to about $v_{eff} = 15.7 \pm 0.2$ cm/ns. For the determination of the speed of light we used the first (largest) TDC peak was used. In order to further investigate the different peaks we also calculated the speed of the light using the second TDC peak of Run 2475. This is shown on Table 7 and it is very similar (within errors) to the value determined from the first peak.

Table 7: Effective Speed of Light.

| Channel No | First Peak | Second Peak | Walk Corrected |
|---|---|---|---|
| | (cm/ns) | (cm/ns) | (cm/ns) |
| 3 | $15.7 \pm 0.5$ | $15.8 \pm 0.5$ | $14.2 \pm 0.5$ |
| 9 | $15.5 \pm 0.5$ | $15.5 \pm 0.5$ | $14.2 \pm 0.5$ |
| 15 | $15.9 \pm 0.4$ | $15.9 \pm 0.4$ | $15.0 \pm 0.6$ |
| Average | $15.70 \pm 0.16$ | $15.73 \pm 0.17$ | $14.5 \pm 0.5$ |

Furthermore, as a second order correction, we investigated the dependence of the TDC value on the energy deposition of the particle, this is known as time walk correction. From the plots it was obvious that for ADC>100, the TDC diminishes but applying to it a simple linear correction the result is almost independent of the ADC. To perform the time walk correction, we used a simple fit to get a straight line. After applying the this correction for the three different blocks we recalculated the speed of light and this is shown on Table 7. This comes out to about 1 ns lower, than the value determined before the WC correction.

## Attenuation Length

### Charged Particle Beam Tests at TRIUMF

### Summer 2001, TRIUMF Beam Test, Bundled Fibers

This work was reported in detail in GlueX-doc-50. The results were: $(283 \pm 2)$ cm, $(273 \pm 3)$ cm and $(234 \pm 3)$ cm for two Kuraray SCSF-81 batches and Pol.Hi.Tech. 0046 multiclad fibers.

### Summer 2005, TRIUMF Beam Test, Module 1

The attenuation length can be extracted by plotting the ADC signal versus the position in Z, with the slope of the straight line in semi-logarithmic scale being the attenuation length. But similar to the case of the Time Difference, taking the Ratio of the means of the Left ADC and the Right ADC reduces the uncertainties and produces a more reliable result. The attenuation length extracted by the Ratio $R$ is shown in Fig. 20. The slope of the curve is the attenuation length itself, and its value for 250 MeV/c positrons is $\lambda = 307 \pm 12$ cm.

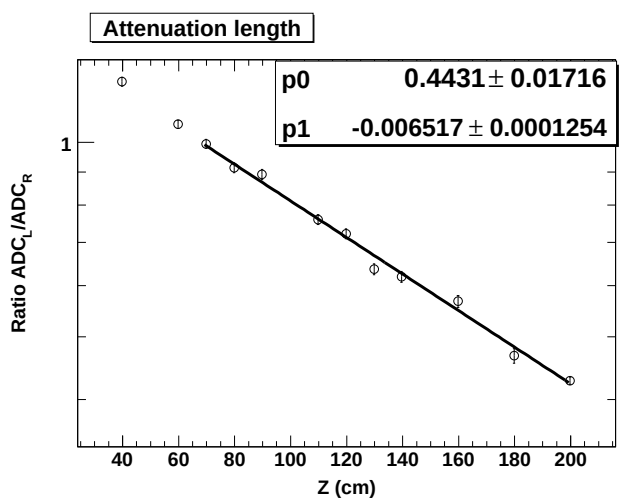


Figure 20: Attenuation length from 120 MeV/c electrons.

Only the region above 60 cm from the module end are fitted, as the contribution of the short attenuation length component is significant below that distance, and the data points obtained are just enough to estimate that this short component is between 30 and 80 cm, as expected for this type of fibers [NOE Calorimeter]. The value obtained from 120 MeV/c positrons is 323 ± 20 cm. The values obtained from the Left or Right ADC data only have larger errors and vary between 260 and 360 cm.

**Cosmic Runs at Regina**

The attenuation length form cosmic runs at Regina was extracted from data taken with bundled fibers (summer 2001), Module 1 (summer 2006) and Module 2 (summer 2007), from single ends and the ratio method of one end over the other. The results are:

- Summer 2001. Bundled fibers were used (i.e. not embedded in a lead matrix). The results were: $(321 \pm 22)$ cm, $(259 \pm 22)$ cm and $(247 \pm 47)$ cm for Kuraray SCSF-81, Pol.Hi.Tech single and multiclad fibers. See GlueX-doc-50 for further details and Table 8 for a summary of the measurements.
- Summer 2006. A single 2" Burle PMT was placed at each end of Module 1, coupled to it via a $10 \times 10$ cm$^2$ light guides. A small trigger counter was placed on top and a large paddle counted under the BCAL. The attenuation length extracted was: $(302.4 \pm 4.1)$ cm, $(303.6 \pm 3.7)$ cm and $(317.1 \pm 2.5)$ cm, from the North, South and ratio, respectively.
- Summer 2007. Two 2" Burle PMT was placed at each end of Module 2, coupled to it via a $10 \times 10$ cm$^2$ light guides, but with only a small $3.8 \times 3.8$ cm$^2$ viewport open in each light guide, one PMT viewing green fibers and the other viewing the blue ones. A small trigger counter was placed on top, a large paddle counted under the BCAL and a small Čerenkov under that. The attenuation length extracted was: $(279.7 \pm 36.4)$ cm, $(240.6 \pm 24.8)$ cm and $(255.3 \pm 19.6)$ cm, from the North, South and ratio, respectively for the green fibers and $(260.5 \pm 17.4)$ cm, $(298.9 \pm 28.4)$ cm and $(271.5 \pm 12.5)$ cm, from the North, South and ratio, respectively for the blue fibers.

More details will be provided during the Calorimetry Workshop held at Jefferson Lab on July 26-28, 2007.

**Cosmic Runs at Hall-B**

**Athens Analysis**

The ADC reading of each readout block was registered and the pedestal was subtracted. Then, the geometric mean of each North and South readout channel was calculated. Most blocks registered comparable pulse heights (PHs) except channel 15 which showed a larger PH.

In order to get an estimate of the energy deposited by comics, we have also summed the ADCs belonging to the same horizontal floor (using the relative gains obtained by Blake) and converted them into energy using the 0.202 calibration factor. The energy sum of a column (laye) shows that on the average a cosmic ray deposits about 110 MeV. The ADC PH was used to determine the attenuation length, to apply cuts and focus on straight through cosmic tracks and to perform the time walk correction on the TDC s readings.

The attenuation length, $\lambda$, is calculated as the slope of the logarithm of the ratio ADC left/ADC right, plotted as a function of the z position namely . The ratio of the ADC values for the different

runs was formed after suppressing the low energy peak and fitted in three different ways: Gaussian fit, Landau fit and no fit at all, taking the mean given by the histogram package. This was done because the first time that $\lambda$ was calculated it seemed too small compared to previous measurements. Nevertheless the dependence is logarithmic so the different fits do not appreciably change the value of $\lambda$. The value of $\lambda$ is $(253 \pm 5)$ cm. This was determined using three different channels, and all gave similar values for $\lambda$.

### Regina Analysis

Significantly unbalanced PMTs require sector-by-sector extraction of the light attenuation length in the BCal. The attenuation length was extracted in two ways: a) from the Mean-Amplitude-vs-Trigger-Position dependences separately for North and South PMTs and b) from the Amplitude-Ratio-vs-Trigger-Position dependences for each segment. The results of both methods are shown in Figure 21: the result from the "one-side" technique was (230.4±2.8 cm) and from the "ratio" technique (235.4±1.7 cm) and are in a good agreement.

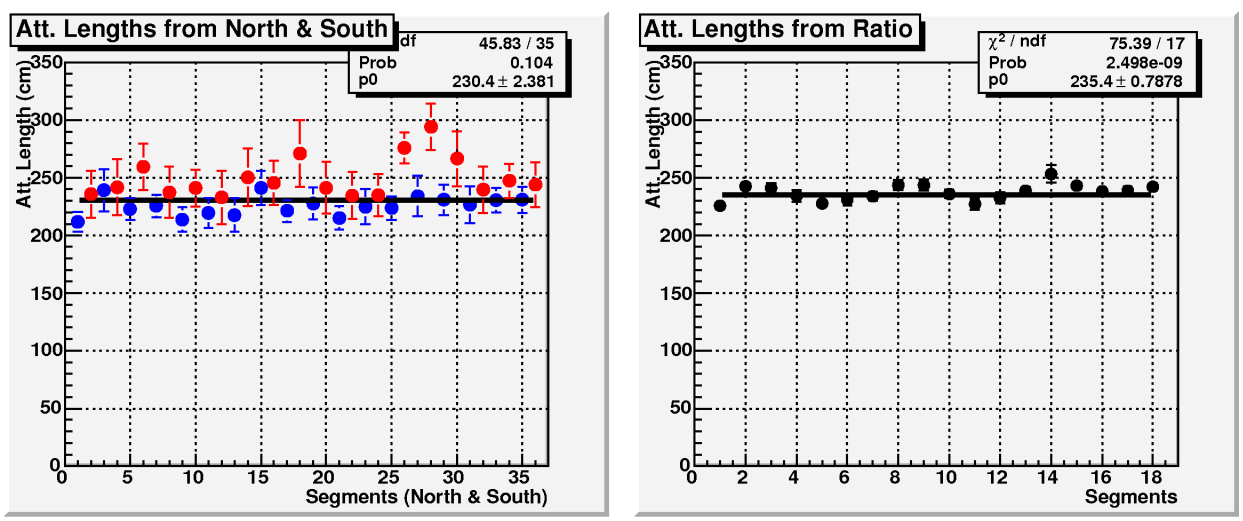


Figure 21: Summary of the attenuation lengths of the light in the BCAL extracted from amplitudes from North or South PMTs (left pannel: blue symbols are for the attenuation length values extracted from the North PMT amplitudes, red symbols are for the values extracted from the South PMT amplitudes; fit made to whole data set) and from the ratio of North/South amplitudes (right panel),

## Number of Photoelectrons

### Charged Particle Beam Test at TRIUMF

This analysis has not been done. It will be carried out in August 2007.

**Cosmic Runs at Regina**

This analysis is under way. Preliminary results will be reported at the Calorimetry Workshop, held at Jefferson Lab, July 26-28, 2007.

**Cosmic Runs at Hall-B**

To select the pedestals in the certain segment in some of the columns, we require the low amplitudes (viz., $adc < 10$) in the 2 remaining segments of the column of interest as well as in all segments of the left neighbour and the right neighbour columns. Abnormal-shaped pedestals were observed in some segments. Run-by-run shifts of pedestals were clearly observed, and all amplitudes in the following analysis were pedestal-corrected on run-by-run basis.

To select the cosmic "muon" (i.e., particle that are close to MIP) tracks in the certain segment in some of the columns, we require the high amplitudes (viz., $adc > 70$) in the two remaining segments of the column of interest as well as low amplitudes (viz., $adc < 10$) in all segments of the left neighbour and the right neighbour columns. Such a criterion suppresses the events with a shower and picks out vertical-oriented particle tracks in the calorimeter; it selects about 15-20% of the total number of events in the run.

The widths of the observed spectra are the result of both the fluctuations in the number of photoelectons (North-South uncorrelated effect) and the variations in the enegry deposited in the calorimeter segment (North-South correlated effect). To remove dependence on the energy variations and extract the mean number of photoelectrons from cosmic "muons", we used the spectra of North/South amplitudes ratio (see Figure **??**). We suppose that each of the amplitude spectra has the Poisson-type shape; consequently, the ratio spectra were fitted to the function (red line in Figure **??**):

$$f(r) \sim \int P(x,\, N_{pe} \cdot \sqrt{R}) \cdot [\frac{1}{r}\, P(\frac{x}{r},\, N_{pe} \,/\, \sqrt{R})]\, [\frac{x}{r}\, dx], \tag{17}$$

where $r$ is a North/South amplitudes ratio, $R$ is an average North/South amplitudes ratio, $N_{pe}$ is the average number of photoelectrons, $P$ is a Poisson-type probability:

$$P(x, N) = e^{-N} \cdot N^x \,/\, \Gamma(x+1), \tag{18}$$

and the $(1/r)$ and $(x/r)$ factors are needed to perform the integration over the uniform $r$-bins.

A summary of the average numbers of photoelectrons extracted sector-by-sector for four cosmics runs is shown in Fig.8. The $N_{pe}$ values of 21.43±1.02, 23.93±0.93, 20.92±0.70, and 20.83±0.75 are extracted from the runs 2458, 2459, 2475, and 2476, correspondingly; these values are in a good agreement. The number of photoelectrons, averaged over all segments and all runs, is 21.56±0.68.

## Summary and Conclusions

The summary of the attenuation length measurements is shown in Table 8 and those for the effective speed of light are displayed in Table 9. Tables on energy and timing resolution will be added in the near future.

This document is a dynamic one. Conclusions will be formulated and written during the Calorimetry Workshop at Jefferson Lab (July 26-28, 2007). Additional analysis is expected to be carried out by the end of 2007, at which time the document will be updated.

| Batch or Test | Fiber Type (mode) | Attenuation Length (cm) | | |
|---|---|---|---|---|
| | | Cosmics | Beam | KLOE |
| Factory | Pol.Hi.Tech.-0046 | 3-5 m | | |
| Factory | Kuraray SCSF-81 | >3.5 m | | |
| Factory | BCF-10 | 2.2 m | | |
| Factory | BCF-12 | 2.7 m | | |
| Factory | BCF-20 | >3.5 m | | |
| 1992 | Bicron BCF-12 | | | 226 ± 3 |
| 1993 | Bicron BCF-12 | | | 286 ± 8 |
| N/A | Kuraray SCSF-81 single–clad | | | 321 ± 5 |
| 1992 | Pol.Hi.Tech.-0046 single–clad | | | 284 ± 5 |
| 1993 | Pol.Hi.Tech.-0046 single–clad | | | 267 ± 6 |
| 2000 | Kuraray SCSF-81 single–clad (loose) | 321 ± 22 | 285 ± 7 | |
| 2000 | Kuraray SCSF-81 single–clad (5/4 stack) | | 283 ± 2 | |
| 2001 | Kuraray SCSF-81 single–clad (5/4 stack) | | 273 ± 3 | |
| 2000 | Pol.Hi.Tech.-0046 single–clad (loose) | 259 ± 20 | | |
| 2000 | Pol.Hi.Tech.-0046 multi–clad (loose) | 247 ± 47 | | |
| 2000 | Pol.Hi.Tech.-0046 multi–clad (5/4 stack) | | 234 ± 3 | |
| 2005 | Pol.Hi.Tech.-0046 (120 Mev/c, Module 1) | | 323 ± 23 | |
| 2005 | Pol.Hi.Tech.-0046 (250 Mev/c, Module 1) | | 307 ± 12 | |
| 2006 | Pol.Hi.Tech.-0046 (North, Module 1) | 302 ± 4 | | |
| 2006 | Pol.Hi.Tech.-0046 (South, Module 1) | 304 ± 4 | | |
| 2006 | Pol.Hi.Tech.-0046 (Ratio, Module 1) | 317 ± 3 | | |
| 2006 | Pol.Hi.Tech.-0046 (Hall-B, Ratio, Module 1) | | 253 ± 5 | |
| 2006 | Pol.Hi.Tech.-0046 (Hall-B, Ratio, Module 1) | | 257 ± 8 | |
| 2007 | Pol.Hi.Tech.-0046 (North, Module 2) | 280 ± 36 | | |
| 2007 | Pol.Hi.Tech.-0046 (South, Module 2) | 241 ± 25 | | |
| 2007 | Pol.Hi.Tech.-0046 (Ratio, Module 2) | 255 ± 20 | | |
| 2007 | BCF-20 (North, Module 2) | 261 ± 17 | | |
| 2007 | BCF-20 (South, Module 2) | 299 ± 28 | | |
| 2007 | BCF-20 (Ratio, Module 2) | 272 ± 13 | | |

Table 8: Attenuation length determined using 2" PMT's from cosmics runs, TRIUMF and Jefferson Lab beam tests. The results are compared to those from KLOE.

| Batch or Test | Fiber Type (mode) | $v_{eff}$ (cm/ns) Cosmics | Beam | KLOE |
|---|---|---|---|---|
| N/A | Kuraray SCSF-81 single–clad (?) | | | 17.2 |
| 2000 | Kuraray SCSF-81 | 19.2 | | |
| 2000 | Pol.Hi.Tech.-0046 | 18.9 | | |
| 2005 | Pol.Hi.Tech.-0046 (120 Mev/c, North, Module 1) | | 15.6 ± 0.4 | |
| 2005 | Pol.Hi.Tech.-0046 (120 Mev/c, South, Module 1) | | 16.8 ± 0.6 | |
| 2005 | Pol.Hi.Tech.-0046 (120 Mev/c, $T_{diff}$, Module 1) | | 16.2 ± 0.4 | |
| 2005 | Pol.Hi.Tech.-0046 (250 Mev/c, North, Module 1) | | 15.9 ± 0.5 | |
| 2005 | Pol.Hi.Tech.-0046 (250 Mev/c, South, Module 1) | | 15.4 ± 0.5 | |
| 2005 | Pol.Hi.Tech.-0046 (250 Mev/c, $T_{diff}$, Module 1) | | 15.7 ± 0.5 | |
| 2006 | Pol.Hi.Tech.-0046 (North, Module 1) | 16.1 ± 1.3 | | |
| 2006 | Pol.Hi.Tech.-0046 (South, Module 1) | 16.0 ± 1.2 | | |
| 2006 | Pol.Hi.Tech.-0046 ($T_{diff}$, Module 1) | 15.8 ± 1 | | |
| 2006 | Pol.Hi.Tech.-0046 (Hall-B, Ratio, Module 1) | | 14.5 ± 0.5 | |

Table 9: Attenuation length determined using 2" PMT's from cosmics runs, TRIUMF and Jefferson Lab beam tests. The results are compared to those from KLOE.

## References


[1] M. Adinolfi et al. Calibration and reconstruction performances of the KLOE electromagnetic calorimeter. *Nucl. Instrum. Meth.*, A461:344–347, 2001.

[2] M. Adinolfi et al. The trigger system of the KLOE experiment. *Nucl. Instrum. Meth.*, A492:134–146, 2002.

[3] M. Adinolfi et al. The KLOE electromagnetic calorimeter. *Nucl. Instrum. Meth.*, A494:326–331, 2002.

[4] M. Adinolfi et al. The KLOE electromagnetic calorimeter. *Nucl. Instrum. Meth.*, A482:364–386, 2002.

[5] A. Aloisio et al. Data acquisition and monitoring for the KLOE detector. *Nucl. Instrum. Meth.*, A516:288–314, 2004.

[6] F. Ambrosino et al. Data handling, reconstruction, and simulation for the KLOE experiment. *Nucl. Instrum. Meth.*, A534:403–433, 2004.

[7] M. Antonelli et al. The adcs and tdcs for the KLOE electromagnetic calorimeter. *Nucl. Instrum. Meth.*, A409:675–678, 1998.

[8] M. Antonelli et al. Quality checks and first calibration of the KLOE electromagnetic calorimeter. *Nucl. Instrum. Meth.*, A409:558–560, 1998.

[9] M.J. Berger and S.M. Seltzer. Tables of energy losses and ranges of electrons and positrons. Technical report, NASA, Washington, DC, 1964.

[10] B. Rossi. *High Energy Particles.* Prentice-Hall, Inc., Engelwood Cliffs, NJ, 1952.

[11] Z. Papandreou. BCAL calorimetry response. Technical report, GlueX Collaboration, 2007. GlueX-doc-840-v1.

[12] Z. Papandreou et al. Request for beam time in Hall B to measure energy and time resolution of the BCAL prototype module. Technical report, GlueX Collaboration, 2006. GlueX-doc-620-v1.

[13] Z. Papandreou and R. Hakobyan. BCAL simulations for the Hall B tests. Technical report, GlueX Collaboration, 2007. GlueX-doc-796-v1.

[14] Z. Papandreou and A. Semenov. Analysis of amplitude information from 2006 bcal cosmics runs. Technical report, GlueX Collaboration, 2007.

[15] R. Hakobyan et al. Simulation of the gluex bcal calorimeter. Technical report, GlueX Collaboration, 2005.

[16] R. Wigmans. On the energy resolution of uranium and other hadron calorimeters. *Nucl. Instrum. Meth.*, A259:389–429, 1987.

[17] A. Antonelli et al. Construction and performance of the lead-scintillating fiber calorimeter prototypes for the kloe detector. *Nucl. Instrum. Meth.*, A354:352–363, 1995.

[18] A. Dzierba. Calibrating BCAL with cosmic rays. Technical report, GlueX Collaboration, 2007. GlueX-doc-834-v1.

[19] C. Kourkoumeli. Analysis of BCAL runs with Pb-converter of different thicknesses. Technical report, GlueX Collaboration, 2007. GlueX-doc-752-v4.

[20] B. Leverington. Sampling fraction fluctuations. Technical report, GlueX Collaboration, 2007. GlueX-doc-827-v2.

[21] U. Amaldi. Fluctuations in calorimetry measurements. *Phys. Scr.*, 23:409–424, 1981.

[22] M. Livan et al. Scintillating-fibre calorimetry. Technical Report CERN-95-02, CERN, 1995.

[23] C.W. Fabjan and F. Gianotti. Calorimetry for particle physics'. Technical Report CERN-EP/2003-075, CERN, 2003.

[24] E. Smith. Specification and evaluation of bcal readout options. Technical report, GlueX Collaboration, 2007. GlueX-doc-795-v9.

[25] D. Lawrence. Calculating BCAL timing resolution. Technical report, GlueX Collaboration, 2007. GlueX-doc-802-v1.

[26] C. Kourkoumeli. Analysis of the cosmic ray runs from the BCAL test at JLab. Technical report, GlueX Collaboration, 2007. GlueX-doc-836-v1.